

## A 38 Million Year Old Mini-Neptune in the Kepler Field

L. G. BOUMA,<sup>1</sup> J. L. CURTIS,<sup>2,3</sup> K. MASUDA,<sup>4</sup> L. A. HILLENBRAND,<sup>5</sup> G. STEFANSSON,<sup>1</sup> A. W. HOWARD,<sup>5</sup>  
H. ISAACSON,<sup>6</sup> N. NARITA,<sup>7,8,9,10</sup> A. FUKUI,<sup>7,10</sup> M. IKOMA,<sup>11</sup> M. TAMURA,<sup>12,9,13</sup> E. FURLAN,<sup>14</sup>  
C. L. GNILKA,<sup>15</sup> K. V. LESTER,<sup>15</sup> AND S. B. HOWELL<sup>15</sup>

<sup>1</sup>Department of Astrophysical Sciences, Princeton University, 4 Ivy Lane, Princeton, NJ 08540, USA

<sup>2</sup>Department of Astronomy, Columbia University, 550 West 120th Street, New York, NY 10027, USA

<sup>3</sup>Department of Astrophysics, American Museum of Natural History, New York, NY 10024, USA

<sup>4</sup>Department of Earth and Space Science, Osaka University, Osaka 560-0043, Japan

<sup>5</sup>Cahill Center for Astrophysics, California Institute of Technology, Pasadena, CA 91125, USA

<sup>6</sup>Astronomy Department, University of California, Berkeley, CA 94720, USA

<sup>7</sup>Komaba Institute for Science, The University of Tokyo, Tokyo 153-8902, Japan

<sup>8</sup>Japan Science and Technology Agency, PRESTO, Tokyo 153-8902, Japan

<sup>9</sup>Astrobiology Center, Tokyo 181-8588, Japan

<sup>10</sup>Instituto de Astrofísica de Canarias (IAC), 38205 La Laguna, Tenerife, Spain

<sup>11</sup>Division of Science, National Astronomical Observatory of Japan, Tokyo 181-8588, Japan

<sup>12</sup>Department of Astronomy, University of Tokyo, Tokyo 113-0033, Japan

<sup>13</sup>National Astronomical Observatory of Japan, Tokyo 181-8588, Japan

<sup>14</sup>NASA Exoplanet Science Institute, Caltech/IPAC, Pasadena, CA 91125, USA

<sup>15</sup>NASA Ames Research Center, Moffett Field, CA 94035, USA

(Received —; Revised —; Accepted —)

Submitted to AAS Journals

### ABSTRACT

Kepler 1627A is a G8V star previously known to host a  $3.3R_{\oplus}$  mini-Neptune on a 7.2 day orbit. The star was observed by the Kepler satellite because it is nearby ( $d = 329 \pm 3$  pc) and it resembles the Sun. Here we show that Kepler 1627 is a member of the  $38^{+6}_{-5}$  Myr old  $\delta$  Lyr cluster using kinematic information from Gaia, stellar rotation periods from TESS, and Li abundances from ground-based spectra. To our knowledge, Kepler 1627Ab is the youngest planet with a precise age yet found by the main Kepler mission. From unresolved starspot-crossing events in the Kepler photometry and a Keck/HIRES transit we find that the planet is likely on an orbit aligned with the stellar spin axis. We also briefly explore the flare arrival time distribution in the short cadence Kepler photometry. The  $\delta$  Lyr cluster is one of many stellar groups whose properties have been clarified using the Gaia data; many other new clusters also overlap with confirmed and candidate exoplanets. Verifying the results of Gaia clustering analyses using TESS rotation periods seems likely to be a path toward expanding the census of age-dated planets, and our understanding of planetary evolution.

**Keywords:** exoplanet evolution (491), stellar associations (1582), open star clusters (1160), stellar ages (1581),

### 1. INTRODUCTION

While thousands of exoplanets have been discovered orbiting nearby stars, the vast majority of them are several billion years old. This makes it

difficult to test origin theories for the different families of planets, since many evolutionary processes are expected to operate on timescales of less than 100 million years.

For instance, the “mini-Neptunes”, thought to be made of molten rocky cores (Kite et al. 2020) and extended atmospheric envelopes of hydrogen and helium, are expected to shrink in size by factors

Corresponding author: L. G. Bouma  
bouma.luke@gmail.com

of several over their first  $10^8$  years (Owen & Wu 2016; Owen 2020). Specifically, they start with sizes of  $4\text{--}12 R_{\oplus}$  shortly after the time of disk dispersal ( $\lesssim 10^7$  years), and shrink to sizes of  $2\text{--}4 R_{\oplus}$  by  $10^8$  years. While the majority of this change is expected to occur within the first few million years of disk dispersal (Owen & Wu 2016), the combination of stellar irradiation and internal heat may also power a more gradual outflow which can eventually deplete or entirely strip the envelope from the rocky core (Owen & Wu 2013; Ginzburg et al. 2018). Discovering young planets, measuring their masses, and detecting their atmospheric outflows are key steps toward testing this paradigm, which is often invoked to explain the observed radius distribution of mature exoplanets (Fulton et al. 2017).

The K2 and TESS missions have now enabled the detection of about ten close-in planets younger than 100 million years, all smaller than Jupiter (Mann et al. 2016; David et al. 2016, 2019; Newton et al. 2019; Bouma et al. 2020; Plavchan et al. 2020; Rizzuto et al. 2020). The Kepler mission however has not yielded any planets with precise ages below one gigayear (Meibom et al. 2013). The reason is that during the main Kepler mission (2009–2013), only four open clusters were known in the Kepler field: NGC 6866, NGC 6811, NGC 6819, and NGC 6791, with ages spanning 0.7 Gyr to 9 Gyr (Meibom et al. 2011). Since that time, analyses of the kinematic, photometric, and astrometric Gaia data have expanded our knowledge of open cluster and moving group memberships (e.g., Cantat-Gaudin et al. 2018; Zari et al. 2018; Kounkel & Covey 2019; Meingast et al. 2021; Kerr et al. 2021). As part of our Cluster Difference Imaging Photometric Survey (CDIPS, Bouma et al. 2019), we concatenated the available analyses from the literature, which yielded a list of candidate young and age-dated stars (see Appendix A).

Comparing our young star list against the Kepler field yielded two discoveries. The first, to be discussed in an upcoming analysis by J. Curtis et al., is that Kepler observed the  $\approx 350$  Myr open cluster Theia 520 (UBC1). At least six Kepler planets are known in the cluster from the Kepler-52 and Kepler-968 systems (Rowe et al. 2014; Jontof-Hutter et al. 2021). The second discovery, and the focus of this work, is that Kepler observed a portion of the  $\delta$  Lyr cluster (Stephenson-1; Theia 73; Stephenson 1959). Figure 1 shows the overlap between the Kepler field and the cluster.

A previous clustering analysis of the Gaia data reported that Kepler 1627 (KIC 6184894; KOI 5245; TIC 120105470) is a member of the  $\delta$  Lyr cluster (Kounkel & Covey 2019). Given the previous statistical validation the close-in mini-Neptune Kepler

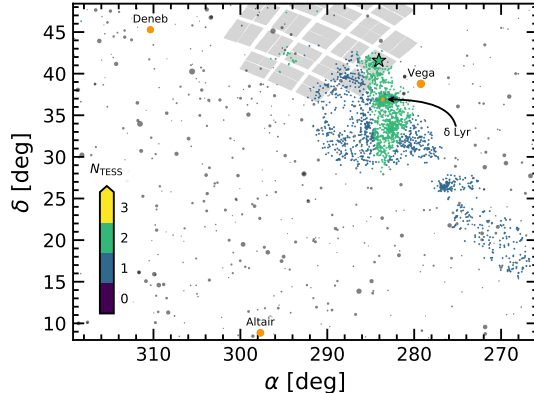


**Figure 1. Kepler and TESS views of the  $\delta$  Lyr cluster.** Colored points are kinematically selected members of the  $\delta$  Lyr cluster. Both Kepler (gray squares) and TESS observed portions of the cluster. Naked-eye stars ( $mv < 6.5$ ) are shown in gray; four of them (orange circles) are annotated. Kepler 1627 (green star) was observed during the entirety of the Kepler mission, and has been observed by TESS for two lunar months to date. The colors of the other cluster members indicate the number of TESS sectors during which they have been observed.

1627b (Tenenbaum et al. 2012; Morton et al. 2016; Thompson et al. 2018), we examined the age of the star and its putative host cluster more closely (Section 2). We find that the  $\delta$  Lyr cluster is  $38^{+6}_{-5}$  Myr old, and that Kepler 1627 is indeed a member of the cluster. Focusing on the planet itself, we confirm that despite the presence of a previously unreported binary companion, the planet orbits the G-dwarf primary on an orbit that appears aligned with the stellar rotation axis (Section 3). We conclude by highlighting broader implications for our ability to age-date a statistical sample of planets (Section 4).

## 2. THE CLUSTER

To assess the age of the cluster and our star of interest, we used a combination of isochronal, gyrochronal, and lithium-based age-dating.

### 2.1. Color-Magnitude Diagram

We measured the isochrone age through an empirical approach. The left panel of Figure 2 shows the color-magnitude diagram (CMD) of stars in the  $\delta$  Lyr cluster, IC 2602, the Pleiades, and the field. The candidate  $\delta$  Lyr cluster members shown are selected based on their positions and kinematics, as discussed in Appendix B. Those from the Pleiades and IC 2602 are adopted from Cantat-Gaudin et al. (2018), and the field stars are from the Gaia EDR3 Catalog of Nearby Stars (Gaia Collaboration et al. 2021). We cleaned these following the data filtering criteria discussed in Appendix B of Gaia Collaboration et al. (2018a), except that we weakened

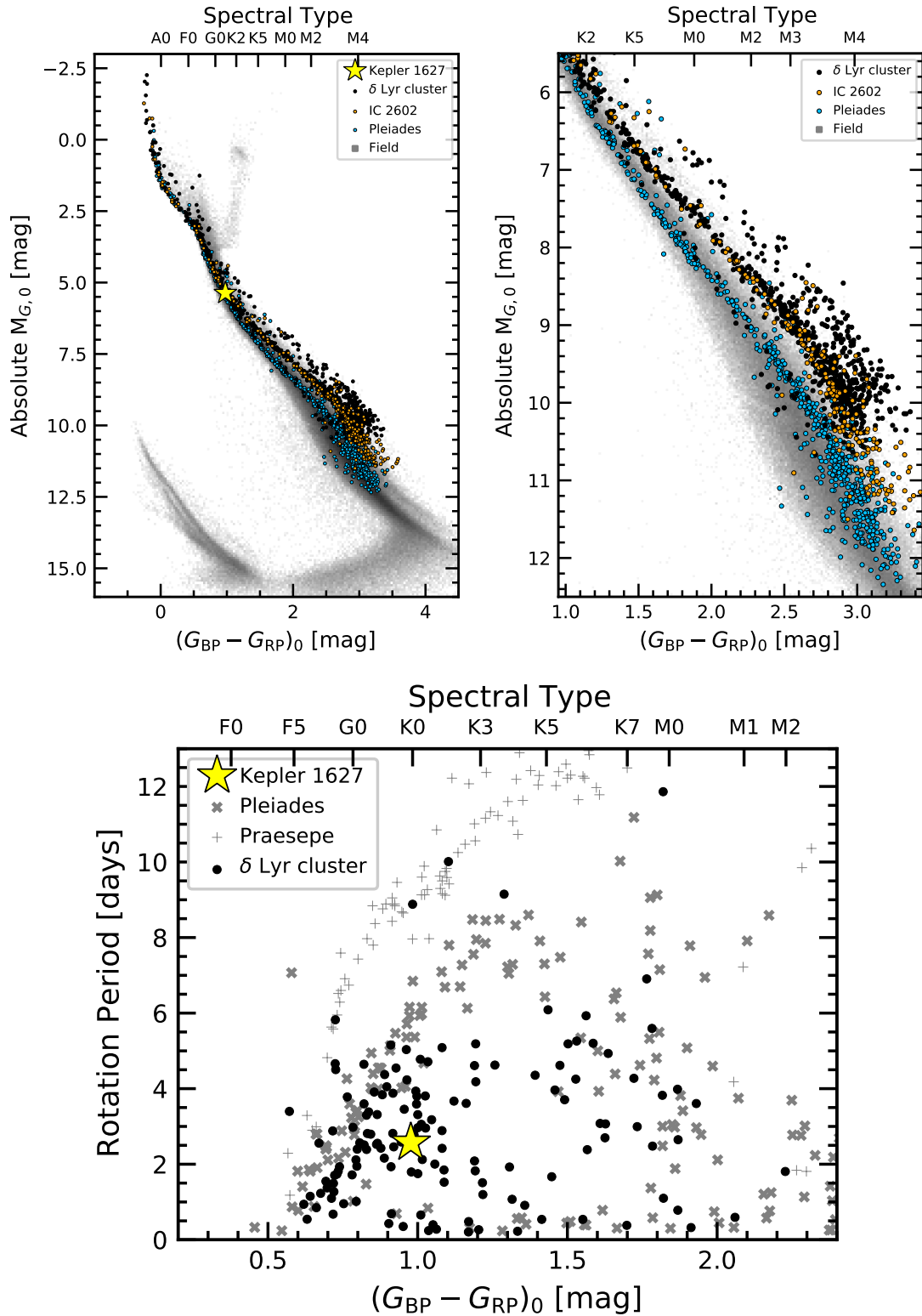


**Figure 2.** The  $\delta$  Lyr cluster is  $38^{+6}_{-5}$  Myr old. *Top:* Color-magnitude diagram of the  $\delta$  Lyr cluster, IC 2602 ( $\approx 35$  Myr), the Pleiades ( $\approx 115$  Myr; Dahm 2015), and the Gaia EDR3 Catalog of Nearby Stars (gray background density; log-stretch). The right panel provides a zoomed view of stars on the pre-main-sequence. The  $\delta$  Lyr cluster and IC 2602 are approximately the same isochronal age. *Bottom:* TESS and Kepler stellar rotation periods versus dereddened Gaia colors, with the Pleiades and Praesepe (650 Myr) shown for reference (Rebull et al. 2016; Douglas et al. 2017). The  $\delta$  Lyr cluster is gyrochronally younger than the Pleiades.

the parallax precision requirement to  $\bar{\omega}/\sigma_{\bar{\omega}} > 5$ . These filters were designed to include genuine binaries while omitting instrumental artifacts. We then corrected for extinction by querying the 3-dimensional maps of Capitanio et al. (2017) and Lallement et al. (2018)<sup>1</sup>, and then applied the extinction coefficients  $k_X \equiv A_X/A_0$  computed by Gaia Collaboration et al. (2018a) and assumed that  $A_0 = 3.1E(B-V)$ . For IC 2602, the Pleiades, and the  $\delta$  Lyr cluster, this procedure yielded a respective mean and standard deviation for the reddening of  $E(B-V) = \{0.020 \pm 0.003, 0.045 \pm 0.008, 0.032 \pm 0.006\}$ . These values agree reasonably well with previously reported values from the literature (e.g., Gaia Collaboration et al. 2018a; Kounkel & Covey 2019; Bossini et al. 2019).

Figure 2 shows that the  $\delta$  Lyr cluster and IC 2602 overlap, and are therefore approximately the same age. In our exploration, we also compared against  $\mu$ -Tau ( $62 \pm 7$  Myr; Gagné et al. 2020) and the Upper-Centaurus-Lupus (UCL) component of the Sco OB2 association ( $\approx 16$  Myr; Pecaut & Mamajek 2016). The pre-main-sequence M dwarfs of the  $\delta$  Lyr cluster were intermediate between these latter two groups. To turn this heuristic interpolation into an age measurement, we used the empirical method developed by Gagné et al. (2020). In brief, we fitted the pre-main-sequence loci of a set of reference clusters, and the locus of the target  $\delta$  Lyr cluster was then modeled as a piecewise linear combination of these reference clusters. For our reference clusters, we adopted members of UCL, IC 2602, and the Pleiades from Damiani et al. (2019) and Cantat-Gaudin et al. (2018) respectively. We removed binaries by requiring  $\text{RUWE} < 1.3$ , `radial_velocity_error` below the 80<sup>th</sup> percentile of each cluster's distribution, and manually excluded stars that were obvious photometric binaries in the CMD. We then passed a moving box average and standard deviation across the CMD in 0.10 mag bins, fitted a univariate spline to the binned values, and assembled a piecewise grid of hybrid isochrones spanning the ages between UCL to the Pleiades following Equations 6 and 7 from Gagné et al. (2020).

The ages returned by this procedure depend on the ages assumed for each reference cluster. We adopted a 115 Myr age for the Pleiades, and a 16 Myr age for UCL (Dahm 2015; Pecaut & Mamajek 2016). The age of IC 2602 however is the most important ingredient, since it receives the most weight in the interpolation. Plausible ages for IC 2602 span 30 Myr to 46 Myr, with slightly older ages being preferred by the lithium-depletion-

boundary (LDB) measurements and younger ages by the main-sequence turn-off (Stauffer et al. 1997; Dobbie et al. 2010; David & Hillenbrand 2015; Randich et al. 2018; Bossini et al. 2019; Bouma et al. 2020). If we were to adopt the 30 Myr age for IC 2602, then the  $\delta$  Lyr cluster would be  $31^{+5}_{-4}$  Myr old. For the converse case of 46 Myr, the  $\delta$  Lyr cluster would be  $44^{+8}_{-7}$  Myr old. We adopt an intermediate 38 Myr age for IC 2602, which yields an age for the  $\delta$  Lyr cluster of  $38^{+6}_{-5}$  Myr.<sup>2</sup> While detailed analyses of the LDB or main-sequence turn-off in the  $\delta$  Lyr cluster could help resolve the tension between the LDB and isochrone ages, these are beyond our scope.

## 2.2. Stellar Rotation Periods

Of the 3,071 candidate  $\delta$  Lyr cluster members reported by Kounkel & Covey (2019), TESS data were available for 924 stars.<sup>3</sup> We extracted light curves from the TESS images using the nearest pixel to each star, and regressed them against systematics with the causal pixel model implemented in the unpopular package (Hattori et al. 2021). We then measured candidate rotation periods using a Lomb-Scargle periodogram (Lomb 1976; Scargle 1982; Astropy Collaboration et al. 2018). To enable cuts on crowding, we queried the Gaia source catalog for stars within a 21."0 radius of the target star (1 TESS pixel). We recorded the number of stars within the aperture with greater brightness than the target star, and with brightness within 1.25 and 2.5 TESS magnitudes of the target star.

We cleaned the candidate TESS rotation period measurements through a combination of automated and manual steps. As a matter of scope, we restricted our attention to the 391 stars discussed in Appendix B in the spatial and kinematic proximity of Kepler 1627. To avoid blending, we also only focused on stars for which no companions were known with a brightness exceeding one-tenth of the target star in a 21."0 radius. There were 192 stars that met these requirements, and that had TESS data available. For plotting purposes we then imposed a selection based on the strength of the signal itself: we required the Lomb Scargle power to exceed 0.2, and the period to be below 15 days.

The lower panel of Figure 2 shows the resulting 145 stars. The majority of these stars fall be-

<sup>2</sup> Our exploration of the PARSEC and MIST isochrone models over a grid of ages, metallicities, and reddenings, yielded the best agreement for this  $\approx 38$  Myr age as well, given  $[\text{Fe}/\text{H}] = +0.1$  and  $A_V = 0.2$  (Bressan et al. 2012; Choi et al. 2016); this preferred CMD reddening is higher than the Lallement et al. (2018) value by a factor of two.

<sup>3</sup> Kepler rotation periods were derived by McQuillan et al. (2014) for 56 stars; in these cases, we adopted the Kepler rotation period.

<sup>1</sup> <https://stilism.obspm.fr/>

low the “slow sequence” of the Pleiades, consistent with a gyrochronological age for the  $\delta$  Lyr cluster below 100 Myr. Approximately 10 stars appear as outliers above the “slow sequence”. Assuming that they are all false positives (*i.e.*, field interlopers), the rotation period detection fraction would be  $135/192 \approx 70\%$ . The rotation periods of other 30 Myr to 50 Myr clusters (*e.g.*, IC 2602 and IC 2391) are indistinguishable (Douglas et al. 2021).

Binarity is known to be an important factor in the density of stars falling underneath the slow sequence (Meibom et al. 2007; Gillen et al. 2020; Bouma et al. 2021). Appendix C discusses this topic, and finds evidence for similar effects to those that have been previously noted in the literature.

### 2.3. Age of Kepler 1627

To summarize, the age of the  $\delta$  Lyr cluster cluster based on the empirical pre-main-sequence interpolation is  $38^{+6}_{-5}$  Myr. This procedure hinges on the age adopted for IC 2602, since it is the closest reference cluster in the color-magnitude diagram. Gyrochronologically, while most of the G and K dwarfs in the  $\delta$  Lyr cluster have not yet converged to a slow sequence, their rotation periods and those of the F dwarfs are also consistent with a 30 to 50 Myr age. The most precise age for Kepler 1627 and its planet are therefore also  $38^{+6}_{-5}$  Myr Myr, based on the star’s spatial, kinematic, and rotational connection to the cluster, and the assumption that the planet formed very quickly after the star.

Beyond the kinematic and rotational lines of evidence for the youth of Kepler 1627, there is a final consistency check: the abundance of Li I as inferred from the 6708 Å doublet (see *e.g.*, Soderblom et al. 2014). We acquired an iodine-free spectrum from Keck/HIRES on the night of 26 March 2021 using the standard setup and reduction techniques of the California Planet Survey (Howard et al. 2010). Following the equivalent width measurement procedure described by Bouma et al. (2021), we find  $\text{EW}_{\text{Li}} = 233^{+5}_{-7}$  mÅ. Note that this value does not correct for the Fe I blend at 6707.44 Å. Given the stellar parameters of Kepler 1627 (Table 1), most notably its effective temperature, this measurement is also in agreement with an age for the star between 30 Myr and 50 Myr (*e.g.*, Randich et al. 2018; Bouma et al. 2021).

## 3. THE PLANET

If the Kepler 1627Ab transit signal is created by a bona fide planet, then to our knowledge its age would make it the youngest planet yet found by

the main Kepler mission.<sup>4</sup> A portion of the light curve is shown with the phase-folded transit in Figure 3. The PDCSAP photometry is dominated by a quasi-periodic starspot signal with a peak-to-peak amplitude that varies between 2% and 8%, depending on the degree of asymmetry in spot coverage between the stellar hemispheres. The starspot signal repeats every  $2.642 \pm 0.042$  days, where the uncertainty is based on the scatter observed between different Kepler quarters. The details of how we model the starspot signal to derive the parameters of the planet are discussed in Appendix D. The stellar parameters are listed in Table 1; the stellar mass, radius, and effective temperature are found by interpolating against a 38 Myr MIST isochrone. The systematic uncertainties are taken to be the difference in parameters from the PARSEC isochrones, and the reported uncertainties are a quadrature sum of the statistical and systematic components. The transit-fitting results, given in Table 2, are consistent with a mini-Neptune sized planet ( $3.34 \pm 0.18 R_{\oplus}$ ) on a close-in circular<sup>5</sup> orbit around a G8V star ( $0.88 \pm 0.02 R_{\odot}$ ).

Could the transit signal be produced by anything other than a planet orbiting this near-solar analog? Morton et al. (2016) validated the planet based on the transit shape, arguing that the most probable false positive scenario was that of a background eclipsing binary, which had a model-dependent probability of  $\approx 10^{-5}$ . As discussed in Appendix E, we discovered a low-mass stellar companion ( $M_B \approx 0.44 M_{\odot}$ ), and so we reconsidered this false positive scenario in some detail.

We identified three new lines of evidence that support the planetary interpretation. First, the transit duration and the orbital period are inconsistent with an eclipsing body around the M-dwarf companion: we find  $\rho_* = 2.00 \pm 0.24 \text{ g cm}^{-3}$ , while the theoretically expected density for the companion is  $\approx 3.2 \text{ g cm}^{-3}$  (Table 2; Choi et al. 2016). The transit duration is therefore too long to explained by a star eclipsing the M dwarf secondary at  $\approx 5\sigma$ .

The second line of confirmatory evidence comes by analyzing the individual Kepler transit times. We isolated each of the 144 observed transits to within  $\pm 4.5$  hr of each transit, and fitted each window with both *i*) a local second-order polynomial and transit, and *ii*) a local linear trend. We let the mid-time of each transit float, and then calculated the residual between the measured mid-time and that of a perfectly periodic orbit. This resid-

<sup>4</sup> The re-purposed K2 mission however has found two younger systems: K2-33b and V1298 Tau (David et al. 2016; Mann et al. 2016; David et al. 2019)

<sup>5</sup> Our transit fitting yields  $e < 0.48$  at  $2\sigma$ ; the constraints on the eccentricity are not particularly strong.

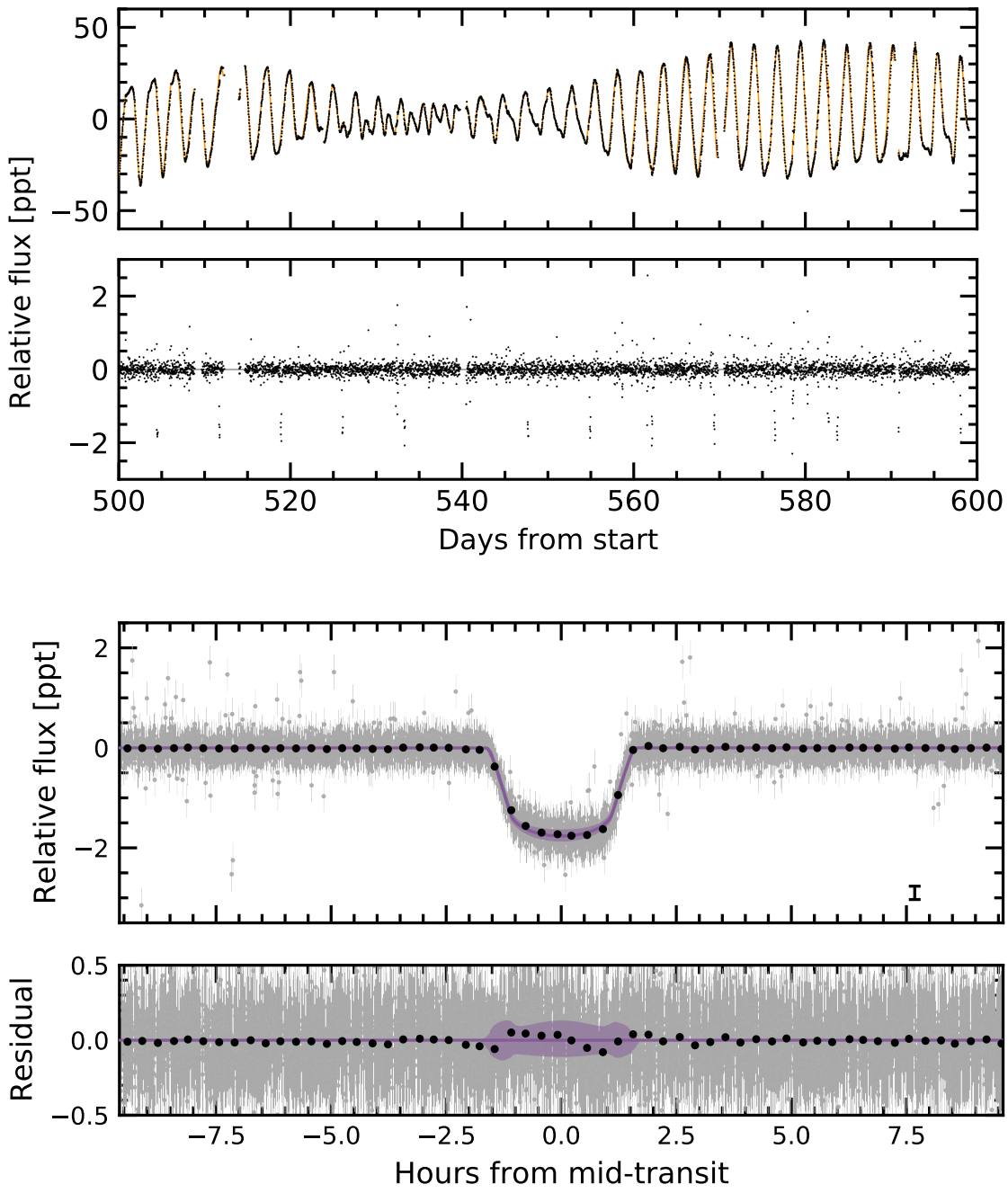


**Figure 3. The light curve of Kepler 1627.** *Top:* The full Kepler dataset spans 1,437 days (3.9 years), sampled at 30 minute cadence. A one hundred day segment is shown here. The *top panel* shows the PDCSAP median-subtracted flux in units of parts-per-thousand ( $\times 10^{-3}$ ). The dominant signal is induced by starspots. The model for the stellar variability (orange line) is subtracted below, revealing the transits of Kepler 1627Ab, as well as other deviations from the model. The Figure Set online shows the entire 3.9 years of observations. *Bottom:* Phase-folded transit of Kepler 1627Ab, with stellar variability removed. The  $2\sigma$  model uncertainties and the maximum *a posteriori* model are shown as the faint purple band, and the dark purple line. Gray points are individual PDCSAP flux measurements; black points are binned to 20 minutes, with a representative error bar shown. The asymmetric residual visible during the transit is robust against detrending methods; we believe it is caused by starspot crossings.

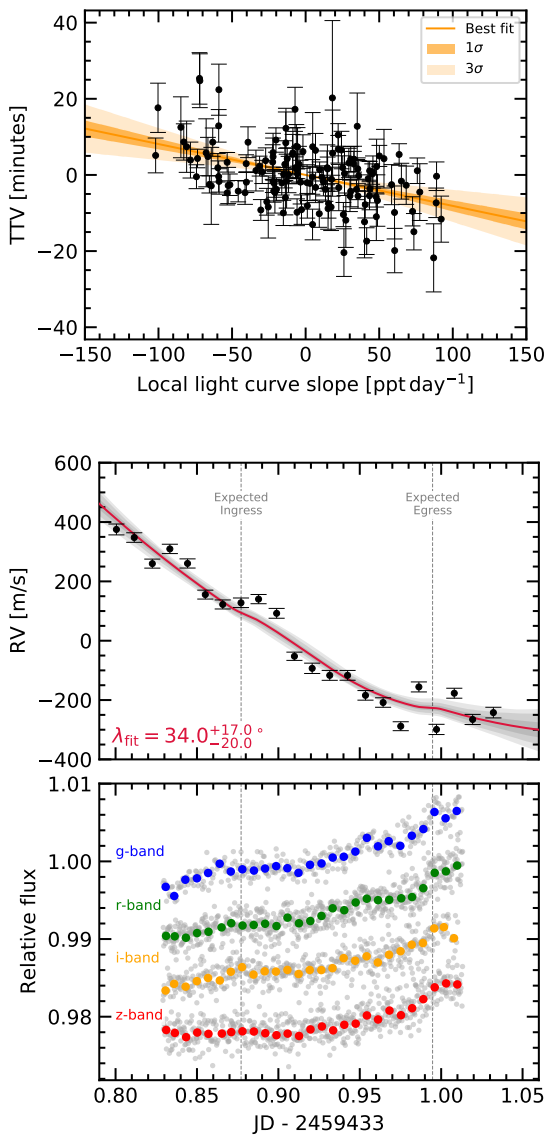


**Figure 4. Evidence for a prograde orbit of Kepler 1627 Ab.** *Top:* The time of each Kepler transit was measured, along with the local slope of the light curve. The two quantities appear anti-correlated, which is most easily explained by starspot crossings during the first (second) half of transit inducing a positive (negative) TTV, provided that the orbit is prograde (Mazeh et al. 2015). The units along the abscissa are most easily understood by considering that the flux from the star changes by  $\sim 60$  ppt per half rotation period ( $\sim 1.3$  days). *Bottom:* Radial velocities from Keck/HIRES during a transit on 7 Aug 2021 UT, observed simultaneously with MuSCAT3 (griz photometry). A quadratic baseline trend was allowed in the RV fit. The best-fit sky-projected obliquity in this model is listed in red; the detection however has marginal statistical significance compared to a “trend-only” model.

ual, the transit timing variation (TTV), is plotted in Figure 4 against the local linear slope. A significant correlation of  $-0.0564 \pm 0.0098 \text{ ppt day}^{-1}$  is observed. Less than ten Kepler Objects of Interest have shown this correlation (Holczer et al. 2015), which is most readily interpreted as a TTV induced by unresolved starspot crossings (Mazeh et al. 2015). This is only possible if the planet transits the primary star, which excludes a background eclipsing binary scenario, and therefore confirms that Kepler 1627Ab is a planet. It also implies that the planet’s orbit is prograde. The latter interpretation assumes that the dominant photometric variability is induced by dark spots, rather than bright faculae (Mazeh et al. 2015). Given the observed transition of Sun-like stellar variability from spot to faculae-dominated regimes, we expect this inference to be reasonably secure (Shapiro et al. 2016; Montet et al. 2017; Reinhold & Hekker 2020).

The final piece of evidence Kepler 1627Ab comes from a spectroscopic transit we measured from Keck/HIRES during the night of 7 Aug 2021 (UT), using the iodine cell for the wavelength calibration. We scheduled the transit using the ephemeris of Holczer et al. (2016), which we verified using the available TESS data. We also acquired simultaneous multi-band photometry using MuSCAT3 to help interpret the radial velocities (Narita et al. 2020). The lower panels in Figure 4 show the results. The photometry shows the expected starspot trend, along with the transit and a likely starspot crossing event at  $\text{JD} - 2459433 = 0.955$ . The radial velocities show significant scatter, and a significant increase in RV is seen shortly after the expected ingress. The internal uncertainties on the RVs ( $\approx 15 \text{ m s}^{-1}$ ) is dominated by the  $v \sin i$  broadening.

We fitted the RVs using the Hirano et al. (2010, 2011) models for the Rossiter-McLaughlin (RM) effect, and allowed the sky-projected obliquity, the stellar equatorial velocity, and the Gaussian dispersion of the spectral lines to vary. We also allowed for an optional linear and quadratic trend, and a white-noise jitter term. The quadratic model with the RM effect is shown in Figure 4; the prior on  $v \sin i$  has been assumed from Table 1. We found  $\chi^2_{\text{red}} = 5.4$  for the best-fitting linear case, and  $\chi^2_{\text{red}} = 4.4$  for the best-fitting quadratic, with a  $\Delta \text{BIC} = \text{BIC}_{\text{line}} - \text{BIC}_{\text{quad}} = 19.6$  and  $\Delta \text{AIC} = \text{AIC}_{\text{line}} - \text{AIC}_{\text{quad}} = 20.6$ . While this provides strong statistical evidence to prefer the quadratic model over the linear one, the  $\chi^2_{\text{red}}$  indicate that neither fit is very good. Considering a quadratic trend alone without any RM effect yields  $\chi^2_{\text{red}} = 4.3$ , and  $\Delta \text{BIC} = \text{BIC}_{\text{trend}} - \text{BIC}_{\text{quad}} = 1.9$  ( $\Delta \text{AIC} = 5.2$ ). From a model-comparison standpoint, there is therefore only weak statistical evidence to pre-

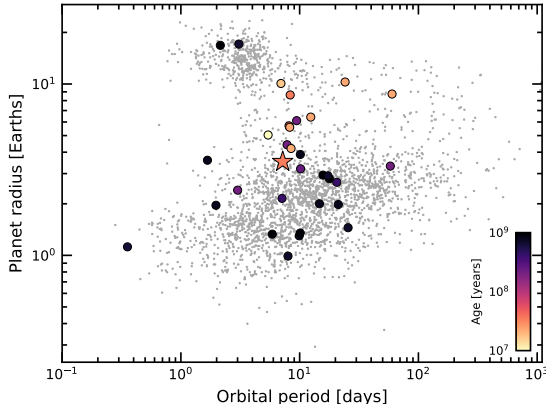


**Figure 5. Radii, orbital periods, and ages of known transiting exoplanets.** Planets older than  $10^9$  years are shown with gray markers. Planets younger than a gigayear with  $\text{Age}/\sigma_{\text{Age}} > 3$  are emphasized. Kepler 1627Ab is shown with a star. The large radii of the youngest transiting planets could be explained by their primordial atmospheres not yet having evaporated; direct measurements of the atmospheric outflows or planetary masses would help to confirm this expectation. Selection effects may also be important. Parameters are from the NASA Exoplanet Archive (July 2, 2021).

fer the best-fitting “RM and quadratic trend” model over the best-fitting “quadratic trend only” model. Given the expected semi-amplitude of the velocity anomaly ( $\Delta v_{\text{RM}} \approx 20 \text{ m s}^{-1}$ ) and the actual achieved precision, the claim of having detected the Doppler transit is marginal at best. From the MuSCAT3 data however, we do know that the transit was observed, and the increase in radial velocity seen shortly after ingress is more consistent with a prograde or polar orbit than a retrograde orbit. Fixing the orbit to be either exactly prograde or exactly retrograde, we find  $\Delta \text{BIC} = \text{BIC}_{\text{retrograde}} - \text{BIC}_{\text{trend}} = 18.0$ ; the retrograde case is ruled out on this basis. More precise data will be needed however to make a more precise obliquity measurement.

#### 4. DISCUSSION & CONCLUSIONS

Kepler 1627Ab provides a new extremum in the ages of the Kepler planets, and opens multiple avenues for further study. More precise observations of the Doppler transit could yield a more precise stellar obliquity, and a means for verifying the expected prograde orbit. Similar transit spectroscopy aimed at detecting either hydrogen or helium absorption could yield insight into the stability of the planet’s atmosphere (e.g., Spake et al. 2018; Vis sapragada et al. 2020). A more challenging measurement would be to determine the planet’s mass, either through detailed timing analyses of the Kepler data, or through a high-cadence multi-color

radial velocity campaign. The mass, measured at sufficient precision, could yield constraints on both the planet’s composition as well as its initial entropy (Owen 2020).

The precision of the Kepler data itself may enable more detailed analyses without needing to acquire more data. While our transit timing study did not yield the detection of any clearly significant planet-planet induced TTVs, the star’s flaring may be suggestive of star-planet interactions. Appendix F highlights an odd flare timing coincidence that may be worthy of further examination.

In the context of the known transiting planets, Kepler 1627Ab is among the youngest known (Figure 5). Comparable systems with precise ages below 100 Myr include K2-33b, DS Tuc Ab, HIP 67522b, TOI 837b, AU Mic b, and the four-planet V1298 Tau system (Mann et al. 2016; David et al. 2016; Newton et al. 2019; David et al. 2019; Bouma et al. 2020; Plavchan et al. 2020). Kepler 1627Ab is currently the smallest of these systems ( $\approx 3.3 R_{\oplus}$ ), which may hint at selection effects in the young planet sample (Zhou et al. 2021). Assuming that these planets have masses between  $\approx 5 M_{\oplus}$  and  $10 M_{\oplus}$ , their large sizes and presumed low densities are in accord with the expectation that mini-Neptunes start their lives with large primordial atmospheres that are shed over the first gigayear (Owen & Wu 2013; Fulton et al. 2017; Ginzburg et al. 2018). Our suggestion of an aligned orbit differs from observed misalignments in number of other close-in mini-Neptunes (Sanchis-Ojeda & Winn 2011; Albrecht et al. 2012; Dalal et al. 2019; Rubenzahl et al. 2021). Unlike these older planets, Kepler 1627Ab seems to have properties consistent with a quiescent disk-driven migration history. The alternative scenario of in-situ formation is disfavored on theoretical grounds: the required disk mass would likely drive migration, and so lacks internal consistency (Inamdar & Schlichting 2015; Ogihara et al. 2015).

Ultimately, the main advance of this work was a precise measurement of the age of Kepler 1627Ab. This age measurement was enabled by identifying the connection of the star to the  $\delta$  Lyr cluster using the Gaia data. Table 3 should enable similar cross-matches to already known planets, as well as forthcoming planets from the TESS mission (Ricker et al. 2015; Guerrero et al. 2021). An alternative path toward age-dating more planets could be to identify kinematic associations around known exoplanet host stars using positions and tangential velocities from Gaia, and to then verify these associations with ancillary rotation periods and spectroscopy (e.g., Tofflemire et al. 2021).

## ACKNOWLEDGMENTS

L.G.B. and J.L.C. are grateful to T. David for help with the transit fitting, to R. Kerr for kindly providing us with the [Kerr et al. \(2021\)](#) membership list prior to its publication. L.G.B., L.H., and N.N. are also grateful to K. Collins for helping resolve the scheduling conflict that would have otherwise prevented the MuSCAT3 observations. L.G.B. acknowledges support by the TESS GI Program, programs G011103 and G022117, through NASA grants 80NSSC19K0386 and 80NSSC19K1728. L.G.B. was also supported by a Charlotte Elizabeth Procter Fellowship from Princeton University. The archival Keck/NIRC2 imaging was acquired by programs 2015A/N301N2L (PI: A. Kraus) and 2019A/N069 (PI: E. Petigura). In addition, this paper is based in part on observations made with the MuSCAT3 instrument, developed by the Astrobiology Center and under financial supports by JSPS KAKENHI (JP18H05439) and JST PRESTO (JPMJPR1775), at Faulkes Telescope North on Maui, HI, operated by the Las Cumbres Observatory. This work is partly supported by JSPS KAKENHI Grant Numbers 22000005, JP15H02063, JP17H04574, JP18H05439, JP18H05442, JST PRESTO Grant Number JPMJPR1775, the Astrobiology Center of National Institutes of Natural Sciences (NINS) (Grant Number AB031010). This paper also includes data collected by the TESS mission, which are publicly available from the Mikulski Archive for Space Telescopes (MAST). Funding for the TESS mission is provided by NASA's Science Mission directorate. We thank the TESS Architects (G. Ricker, R. Vanderspek, D. Latham, S. Seager, J. Jenkins) and the many TESS team members for their efforts to make the mission a continued success. Finally, this research has made use of the Keck Observatory Archive (KOA), which is operated by the W. M. Keck Observatory and the NASA Exoplanet Science Institute (NExSci), under contract with the National Aeronautics and Space Administration. We also thank the Keck Observatory staff for their support of HIRES and remote observing. We recognize the importance that the summit of Maunakea has within the indigenous Hawaiian community, and are deeply grateful to have the opportunity to conduct observations from this mountain.

*Software:* astrobase ([Bhatti et al. 2018](#)), astropy ([Astropy Collaboration et al. 2018](#)), astroquery ([Ginsburg et al. 2018](#)), corner ([Foreman-Mackey 2016](#)), exoplanet ([Foreman-Mackey et al. 2020](#)), and its dependencies ([Agol](#)

et al. 2020; Kipping 2013; Luger et al. 2019; Theano Development Team 2016), IPython ([Pérez & Granger 2007](#)), matplotlib ([Hunter 2007](#)), numpy ([Walt et al. 2011](#)), pandas ([McKinney 2010](#)), PyMC3 ([Salvatier et al. 2016](#)), scipy ([Jones et al. 2001](#)), TESS-point ([Burke et al. 2020](#)), wotan ([Hippke et al. 2019](#)).

*Facilities:* *Astrometry:* Gaia ([Gaia Collaboration et al. 2018b, 2020](#)). *Imaging:* Second Generation Digitized Sky Survey. Keck:II (NIRC2; [www2.keck.hawaii.edu/inst/nirc2](#)). Gemini:North ('Alopeke; [Scott et al. 2018](#)). *Spectroscopy:* Keck:I (HIRES; [Vogt et al. 1994](#)). *Photometry:* Kepler ([Borucki et al. 2010](#)), MuSCAT3 ([Narita et al. 2020](#)), TESS ([Ricker et al. 2015](#)).

**Table 1.** Literature and Measured Properties for Kepler 1627

Primary Star			
TIC 120105470			
GAIADR2 <sup>†</sup> 2103737241426734336			
Parameter	Description	Value	Source
$\alpha_{J2015.5}$ .....	Right Ascension (hh:mm:ss) .....	18:56:13.6	1
$\delta_{J2015.5}$ .....	Declination (dd:mm:ss) .....	+41:34:36.22	1
V .....	Johnson V mag. ....	13.11 $\pm$ 0.08	2
G .....	Gaia G mag. ....	13.05 $\pm$ 0.02	1
T .....	TESS T mag. ....	12.53 $\pm$ 0.02	2
J .....	2MASS J mag. ....	11.69 $\pm$ 0.02	3
H .....	2MASS H mag. ....	11.30 $\pm$ 0.02	3
K <sub>S</sub> .....	2MASS K <sub>S</sub> mag. ....	11.19 $\pm$ 0.02	3
$\pi$ .....	Gaia EDR3 parallax (mas) .....	3.009 $\pm$ 0.032	1
$d$ .....	Distance (pc) .....	329.5 $\pm$ 3.5	1, 4
$\mu_\alpha$ .....	Gaia EDR3 proper motion .....	1.716 $\pm$ 0.034	1
	in RA (mas yr <sup>-1</sup> )		
$\mu_\delta$ .....	Gaia EDR3 proper motion .....	-1.315 $\pm$ 0.034	1
	in DEC (mas yr <sup>-1</sup> )		
RUWE .....	Gaia EDR3 renormalized .....	2.899	1
	unit weight error		
RV .....	Systemic radial velocity (km s <sup>-1</sup> ) .....	-14.3 $\pm$ 1.0	5
Spec. Type .....	Spectral Type .....	G8V	5
$v \sin i_*$ .....	Rotational velocity (km s <sup>-1</sup> ) .....	18.9 $\pm$ 1.0	5
Li EW .....	6708Å Equiv. Width (mÅ) .....	233 <sup>+5</sup> <sub>-7</sub>	5
$T_{\text{eff}}$ .....	Effective Temperature (K) .....	5505 $\pm$ 60	6
$\log g_*$ .....	Surface Gravity (cgs) .....	4.53 $\pm$ 0.05	6
$R_*$ .....	Stellar radius ( $R_\odot$ ) .....	0.881 $\pm$ 0.018	6
$M_*$ .....	Stellar mass ( $R_\odot$ ) .....	0.953 $\pm$ 0.019	6
$A_V$ .....	Interstellar reddening (mag) .....	0.2 $\pm$ 0.1	6
[Fe/H] .....	Metallicity .....	0.1 $\pm$ 0.1	6
$P_{\text{rot}}$ .....	Rotation period (d) .....	2.642 $\pm$ 0.042	7
Age .....	Adopted stellar age (Myr) .....	38 <sup>+6</sup> <sub>-5</sub>	8
$\rho_B$	Apparent separation of .....	0.16 $\pm$ 0.02	9
	primary and secondary (as)		
$\theta_B$	Separation angle (deg) .....	91.9 $\pm$ 2.5	9
$\Delta m_{832}$	Mag difference ('Alopeke 832 nm)	3.1 $\pm$ 0.1	9
$\Delta m_{Kp}$	Mag difference (NIRC2 Kp) .....	2.5 $\pm$ 0.2	10
$\rho_B$	Apparent separation of .....	53 $\pm$ 7	1, 4, 9
	primary and secondary (AU)		

NOTE—<sup>†</sup> The GAIADR2 and GAIAEDR3 identifiers for Kepler 1627A are identical. The secondary is not resolved in the Gaia point source catalog. Provenances are: <sup>1</sup>Gaia Collaboration et al. (2018), <sup>2</sup>Stassun et al. (2019), <sup>3</sup>Skrutskie et al. (2006), <sup>4</sup>Lindgren et al. (2021), <sup>5</sup>Hires spectra and Yee et al. (2017), <sup>6</sup>Cluster isochrone (MIST adopted; PARSEC compared for quoted uncertainty), <sup>7</sup>Kepler light curve, <sup>8</sup>Pre-main-sequence CMD interpolation (Section 2.1), <sup>9</sup>'Alopeke imaging 2021-06-24, <sup>10</sup>NIRC2 imaging 2015-07-22.

**Table 2.** Priors and Posteriors for Model Fitted to the Long Cadence Kepler 1627b Light Curve.

Param.	Unit	Prior	Median	Mean	Std. Dev.	3%	97%	ESS	$\hat{R} - 1$
<i>Sampled</i>									
$P$	d	$\mathcal{N}(7.20281; 0.01000)$	7.2028039	7.2028039	0.0000074	7.2027901	7.2028180	8673	0.0008753
$t_0^{(1)}$	d	$\mathcal{N}(120.79053; 0.02000)$	120.7904073	120.7904027	0.0009503	120.7886845	120.7922021	6349	0.0005352
$\log R_p/R_\star$	–	$\mathcal{U}(-4.605; 0.000)$	-3.36501	-3.36176	0.04060	-3.43579	-3.28478	2217	0.00138
$b$	–	$\mathcal{U}(0; 1 + R_p/R_\star)$	0.4638	0.4386	0.1994	0.0011	0.7415	1273	0.0015
$u_1$	–	Kipping (2013)	0.27	0.293	0.184	0.	0.613	3534	0.001
$u_2$	–	Kipping (2013)	0.422	0.385	0.317	-0.213	0.901	3486	0.001
$R_\star$	$R_\odot$	$\mathcal{T}(0.881; 0.018)$	0.881	0.881	0.018	0.844	0.913	6920	-0.
$\log g$	cgs	$\mathcal{N}(4.530; 0.050)$	4.531	4.532	0.051	4.438	4.628	7262	0.
$\langle f \rangle$	–	$\mathcal{N}(0.500; 0.100)$	0.4999	0.4999	0.0001	0.4997	0.5	8553	0.0002
$e^{(2)}$	–	Van Eylen et al. (2019)	0.147	0.181	0.152	0.	0.456	1954	0.001
$\omega$	rad	$\mathcal{U}(0.000; 6.283)$	0.097	0.058	1.840	-2.867	3.141	3805	0.001
$\log \sigma_f$	–	$\mathcal{N}(\log \langle \sigma_f \rangle; 2.000)$	-8.034	-8.034	0.008	-8.048	-8.020	7639	0.
$\sigma_{\text{rot}}$	$d^{-1}$	InvGamma(1.000; 5.000)	0.07	0.07	0.001	0.068	0.072	8198	0.001
$\log P_{\text{rot}}$	$\log(d)$	$\mathcal{N}(0.958; 0.020)$	0.978	0.978	0.001	0.975	0.980	7991	0.
$\log Q_0$	–	$\mathcal{N}(0.000; 2.000)$	-0.325	-0.325	0.043	-0.407	-0.246	8304	0.002
$\log dQ$	–	$\mathcal{N}(0.000; 2.000)$	7.699	7.697	0.103	7.505	7.888	8140	0.001
$f$	–	$\mathcal{U}(0.010; 1.000)$	0.01	0.01	0.	0.01	0.01	5097	0.002
<i>Derived</i>									
$R_p/R_\star$	–	–	0.035	0.035	0.001	0.032	0.037	2217	0.001
$\rho_\star$	$\text{g cm}^{-3}$	–	1.984	2.001	0.236	1.573	2.450	7248	0.
$R_p$	$R_{\text{Jup}}$	–	0.297	0.298	0.016	0.269	0.330	3047	0.001
$a/R_\star$	–	–	17.589	17.611	0.691	16.280	18.870	7247	0.
$\cos i$	–	–	0.027	0.025	0.010	0.003	0.039	1435	0.002
$T_{14}$	hr	–	2.825	2.826	0.057	2.717	2.927	4099	0.001
$T_{13}$	hr	–	2.575	2.562	0.086	2.415	2.710	2190	-0.

NOTE— ESS refers to the number of effective samples.  $\hat{R}$  is the Gelman-Rubin convergence diagnostic. Logarithms through this table are in base- $e$ .  $\mathcal{U}$  denotes a uniform distribution,  $\mathcal{N}$  a normal distribution, and  $\mathcal{T}$  a truncated normal bounded between zero and an upper limit much larger than the mean.

(1) The ephemeris is in units of BJDTDB - 2454833. (2) The eccentricity vectors are sampled in the  $(e \cos \omega, e \sin \omega)$  basis.

**Table 3.** Young, Age-dated, and Age-dateable Stars Within the Nearest Few Kiloparsecs.

Parameter	Example Value	Description
source_id	1709456705329541504	Gaia DR2 source identifier.
ra	247.826	Gaia DR2 right ascension [deg].
dec	79.789	Gaia DR2 declination [deg].
parallax	35.345	Gaia DR2 parallax [mas].
parallax_error	0.028	Gaia DR2 parallax uncertainty [mas].
pmra	94.884	Gaia DR2 proper motion $\mu_\alpha \cos \delta$ [mas yr $^{-1}$ ].
pmdec	-86.971	Gaia DR2 proper motion $\mu_\delta$ [mas yr $^{-1}$ ].
phot_g_mean_mag	6.85	Gaia DR2 $G$ magnitude.
phot_bp_mean_mag	6.409	Gaia DR2 $G_{\text{BP}}$ magnitude.
phot_rp_mean_mag	7.189	Gaia DR2 $G_{\text{RP}}$ magnitude.
cluster	NASAExoArchive_ps_20210506,Uma,IR_excess	Comma-separated cluster or group name.
age	9.48,nan,nan	Comma-separated logarithm (base-10) of reported <sup>a</sup> age in years.
mean_age	9.48	Mean (ignoring NaNs) of age column.
reference_id	NASAExoArchive_ps_20210506,Ujjwal2020,CottenSong2016	Comma-separated provenance of group membership.
reference_bibcode	2013PASP..125..989A,2020AJ....159..166U,2016ApJS..225..15C	ADS bibcode corresponding to reference_id.

NOTE— Table 3 is published in its entirety in a machine-readable format. This table is a concatenation of the studies listed in Table 4. One entry is shown for guidance regarding form and content. In this particular example, the star has a cold Jupiter on a 16 year orbit, HD 150706b (Boisse et al. 2012). An infrared excess has been reported (Cotten & Song 2016), and the star was identified by Ujjwal et al. (2020) as a candidate UMa moving group member ( $\approx 400$  Myr; Mann et al. 2020). The star's RV activity and TESS rotation period corroborate its youth.

**Table 4.** Provenances of Young and Age-dateable Stars.

Reference	$N_{\text{Gaia}}$	$N_{\text{Age}}$	$N_{G_{\text{RP}} < 16}$
Kounkel et al. (2020)	987376	987376	775363
Cantat-Gaudin & Anders (2020)	433669	412671	269566
Cantat-Gaudin et al. (2018)	399654	381837	246067
Kounkel & Covey (2019)	288370	288370	229506
Cantat-Gaudin et al. (2020)	233369	227370	183974
Zari et al. (2018) UMS	86102	0	86102
Wenger et al. (2000) Y*?	61432	0	45076
Zari et al. (2018) PMS	43719	0	38435
Gaia Collaboration et al. (2018a) $d > 250 \text{ pc}$	35506	31182	18830
Castro-Ginard et al. (2020)	33635	24834	31662
Kerr et al. (2021)	30518	25324	27307
Wenger et al. (2000) Y*○	28406	0	16205
Villa Vélez et al. (2018)	14459	14459	13866
Cantat-Gaudin et al. (2019)	11843	11843	9246
Damiani et al. (2019) PMS	10839	10839	9901
Oh et al. (2017)	10379	0	10370
Meingast et al. (2021)	7925	7925	5878
Wenger et al. (2000) pMS*	5901	0	3006
Gaia Collaboration et al. (2018a) $d < 250 \text{ pc}$	5378	817	3968
Kounkel et al. (2018)	5207	3740	5207
Ratzenböck et al. (2020)	4269	4269	2662
Wenger et al. (2000) TT*	4022	0	3344
Damiani et al. (2019) UMS	3598	3598	3598
Rizzuto et al. (2017)	3294	3294	2757
Akeson et al. (2013)	3107	868	3098
Tian (2020)	1989	1989	1394
Goldman et al. (2018)	1844	1844	1783
Cotten & Song (2016)	1695	0	1693
Gagné et al. (2018b)	1429	0	1389
Röser & Schilbach (2020) Psc-Eri	1387	1387	1107
Röser & Schilbach (2020) Pleiades	1245	1245	1019
Wenger et al. (2000) TT?	1198	0	853
Gagné & Faherty (2018)	914	0	913
Pavlidou et al. (2021)	913	913	504
Gagné et al. (2018a)	692	0	692
Ujjwal et al. (2020)	563	0	563
Gagné et al. (2020)	566	566	351
Esplin & Luhman (2019)	377	443	296
Roccatagliata et al. (2020)	283	283	232
Meingast & Alves (2019)	238	238	238
Fürnkranz et al. (2019) Coma-Ber	214	214	213
Fürnkranz et al. (2019) Neighbor Group	177	177	167
Kraus et al. (2014)	145	145	145

NOTE— Table 4 describes the provenances for the young and age-dateable stars in Table 3.  $N_{\text{Gaia}}$ : number of Gaia stars we parsed from the literature source.  $N_{\text{Age}}$ : number of stars in the literature source with ages reported.  $N_{G_{\text{RP}} < 16}$ : number of Gaia stars we parsed from the literature source with either  $G_{\text{RP}} < 16$ , or a parallax S/N exceeding 5 and a distance closer than 100 pc. The latter criterion included a few hundred white dwarfs that would have otherwise been neglected. Some studies are listed multiple times if they contain multiple tables. Wenger et al. (2000) refers to the SIMBAD database.

## REFERENCES

- Agol, E., Luger, R., & Foreman-Mackey, D. 2020, *AJ*, **159**, 123
- Akeson, R. L., Chen, X., Ciardi, D., et al. 2013, *PASP*, **125**, 989
- Albrecht, S., Winn, J. N., Johnson, J. A., et al. 2012, *ApJ*, **757**, 18
- Astropy Collaboration, Price-Whelan, A. M., Sipőcz, B. M., et al. 2018, *AJ*, **156**, 123
- Beaumont, C., Robitaille, T., Borkin, M., & Goodman, A. 2014, glueviz v0.4: multidimensional data exploration
- Bhatti, W., Bouma, L. G., & Wallace, J. 2018, astrobase, <https://doi.org/10.5281/zenodo.1469822>
- Boisse, I., Pepe, F., Perrier, C., et al. 2012, *A&A*, **545**, A55
- Borucki, W. J., Koch, D., Basri, G., et al. 2010, *Science*, **327**, 977
- Bossini, D., Vallenari, A., Bragaglia, A., et al. 2019, *A&A*, **623**, A108
- Bouma, L. G., Curtis, J. L., Hartman, J. D., Winn, J. N., & Bakos, G. A. 2021, arXiv:2107.08050 [astro-ph], arXiv: 2107.08050
- Bouma, L. G., Hartman, J. D., Bhatti, W., Winn, J. N., & Bakos, G. Á. 2019, *ApJS*, **245**, 13
- Bouma, L. G., Hartman, J. D., Brahm, R., et al. 2020, *AJ*, **160**, 239
- Bressan, A., Marigo, P., Girardi, L., et al. 2012, *MNRAS*, **427**, 127
- Burke, C. J., Levine, A., Fausnaugh, M., et al. 2020, TESS-Point: High precision TESS pointing tool, Astrophysics Source Code Library, ascl:2003.001
- Cantat-Gaudin, T., & Anders, F. 2020, *A&A*, **633**, A99
- Cantat-Gaudin, T., Jordi, C., Vallenari, A., et al. 2018, *A&A*, **618**, A93
- Cantat-Gaudin, T., Jordi, C., Vallenari, A., et al. 2018, *A&A*, **618**, A93
- Cantat-Gaudin, T., Jordi, C., Wright, N. J., et al. 2019, *A&A*, **626**, A17
- Cantat-Gaudin, T., Anders, F., Castro-Ginard, A., et al. 2020, *A&A*, **640**, A1
- Capitanio, L., Lallement, R., Vergely, J. L., Elyajouri, M., & Monreal-Ibero, A. 2017, *A&A*, **606**, A65
- Castro-Ginard, A., Jordi, C., Luri, X., et al. 2020, *A&A*, **635**, A45
- Choi, J., Dotter, A., Conroy, C., et al. 2016, *ApJ*, **823**, 102
- Cotten, T. H., & Song, I. 2016, *ApJS*, **225**, 15
- Dahm, S. E. 2015, *ApJ*, **813**, 108, aDS Bibcode: 2015ApJ...813..108D
- Dai, F., Winn, J. N., Berta-Thompson, Z., Sanchis-Ojeda, R., & Albrecht, S. 2018, *AJ*, **155**, 177
- Dalal, S., Hébrard, G., Lecavelier des Étangs, A., et al. 2019, *A&A*, **631**, A28
- Damiani, F., Prisinzano, L., Pillitteri, I., Micela, G., & Sciortino, S. 2019, *A&A*, **623**, A112, publisher: EDP Sciences
- Damiani, F., Prisinzano, L., Pillitteri, I., Micela, G., & Sciortino, S. 2019, *A&A*, **623**, A112
- Davenport, J. R. A. 2016, *ApJ*, **829**, 23, aDS Bibcode: 2016ApJ...829...23D
- Davenport, J. R. A., Hawley, S. L., Hebb, L., et al. 2014, *ApJ*, **797**, 122, aDS Bibcode: 2014ApJ...797..122D
- David, T., Hillenbrand, L., & Petigura, E. 2016, *Nature*, **534**, 658
- David, T. J., & Hillenbrand, L. A. 2015, *ApJ*, **804**, 146
- David, T. J., Petigura, E. A., Luger, R., et al. 2019, *ApJL*, **885**, L12
- Dias, W. S., Monteiro, H., Caetano, T. C., et al. 2014, *Astronomy and Astrophysics*, **564**, A79
- Dobbie, P. D., Lodieu, N., & Sharp, R. G. 2010, *MNRAS*, **409**, 1002
- Douglas, S. T., Agüeros, M. A., Covey, K. R., & Kraus, A. 2017, *ApJ*, **842**, 83
- Douglas, S. T., Pérez Chávez, J., Cargile, P. A., et al. 2021, Constraining Stellar Rotation at the ZAMS
- Eggen, O. J. 1968, *The Astrophysical Journal*, **152**, 77
- Esplin, T. L., & Luhman, K. L. 2019, *AJ*, **158**, 54
- Foreman-Mackey, D. 2016, *Journal of Open Source Software*, **1**, 24
- Foreman-Mackey, D., Czekala, I., Luger, R., et al. 2020, exoplanet-dev/exoplanet v0.2.6
- Fulton, B. J., Petigura, E. A., Howard, A. W., et al. 2017, *AJ*, **154**, 109
- Fürnkranz, V., Meingast, S., & Alves, J. 2019, *A&A*, **624**, L11
- Gagné, J., David, T. J., Mamajek, E. E., et al. 2020, *ApJ*, **903**, 96
- Gagné, J., & Faherty, J. K. 2018, *ApJ*, **862**, 138
- Gagné, J., Roy-Loubier, O., Faherty, J. K., Doyon, R., & Malo, L. 2018a, *ApJ*, **860**, 43
- Gagné, J., Mamajek, E. E., Malo, L., et al. 2018b, *ApJ*, **856**, 23
- Gagné, J., David, T. J., Mamajek, E. E., et al. 2020, *ApJ*, **903**, 96
- Gaia Collaboration, Brown, A. G. A., Vallenari, A., et al. 2020, arXiv e-prints, arXiv:2012.01533

- Gaia Collaboration, Babusiaux, C., van Leeuwen, F., et al. 2018a, *A&A*, **616**, A10
- Gaia Collaboration, Brown, A. G. A., Vallenari, A., et al. 2018b, *A&A*, **616**, A1
- Gaia Collaboration, Smart, R. L., Sarro, L. M., et al. 2021, *A&A*, **649**, A6
- Gelman, A., & Rubin, D. B. 1992, *Statistical Science*, **7**, 457, publisher: Institute of Mathematical Statistics
- Gillen, E., Briegal, J. T., Hodgkin, S. T., et al. 2020, *MNRAS*, **492**, 1008
- Ginsburg, A., Sipocz, B., Madhura Parikh, et al. 2018, *Astropy/Astroquery: V0.3.7 Release*
- Ginzburg, S., Schlichting, H. E., & Sari, R. 2018, *MNRAS*, **476**, 759
- Goldman, B., Röser, S., Schilbach, E., Moór, A. C., & Henning, T. 2018, *ApJ*, **868**, 32
- Guerrero, N. M., Seager, S., Huang, C. X., et al. 2021, *arXiv:2103.12538 [astro-ph]*, arXiv: 2103.12538
- Hattori, S., Foreman-Mackey, D., Hogg, D. W., et al. 2021, arXiv e-prints, arXiv:2106.15063
- Hippke, M., David, T. J., Mulders, G. D., & Heller, R. 2019, *AJ*, **158**, 143
- Hirano, T., Suto, Y., Taruya, A., et al. 2010, *ApJ*, **709**, 458
- Hirano, T., Suto, Y., Winn, J. N., et al. 2011, *ApJ*, **742**, 69, aDS Bibcode: 2011ApJ...742...69H
- Hoffman, M. D., & Gelman, A. 2014, *Journal of Machine Learning Research*, **15**, 1593
- Holczer, T., Shporer, A., Mazeh, T., et al. 2015, *ApJ*, **807**, 170
- Holczer, T., Mazeh, T., Nachmani, G., et al. 2016, *ApJS*, **225**, 9
- Howard, A. W., Johnson, J. A., Marcy, G. W., et al. 2010, *ApJ*, **721**, 1467
- Hunter, J. D. 2007, *Computing in Science & Engineering*, **9**, 90
- Ilin, E., Schmidt, S. J., Poppenhöger, K., et al. 2021, *A&A*, **645**, A42
- Inamdar, N. K., & Schlichting, H. E. 2015, *MNRAS*, **448**, 1751
- Jones, E., Oliphant, T., Peterson, P., et al. 2001, Open source scientific tools for Python
- Jontof-Hutter, D., Wolfgang, A., Ford, E. B., et al. 2021, *AJ*, **161**, 246
- Kerr, R., Rizzuto, A. C., Kraus, A. L., & Offner, S. S. R. 2021, *arXiv:2105.09338 [astro-ph]*, arXiv: 2105.09338
- Kharchenko, N. V., Piskunov, A. E., Schilbach, E., Röser, S., & Scholz, R.-D. 2013, *A&A*, **558**, A53
- Kipping, D. M. 2013, *MNRAS*, **435**, 2152
- Kite, E. S., Fegley, Jr., B., Schaefer, L., & Ford, E. B. 2020, *ApJ*, **891**, 111
- Kounkel, M., & Covey, K. 2019, *AJ*, **158**, 122
- Kounkel, M., & Covey, K. 2019, *AJ*, **158**, 122
- Kounkel, M., Covey, K., & Stassun, K. G. 2020, *AJ*, **160**, 279
- Kounkel, M., Covey, K., Suárez, G., et al. 2018, *AJ*, **156**, 84
- Kounkel, M., Covey, K., Suárez, G., et al. 2018, *AJ*, **156**, 84
- Kraus, A. L., Shkolnik, E. L., Allers, K. N., & Liu, M. C. 2014, *AJ*, **147**, 146
- Lallement, R., Capitanio, L., Ruiz-Dern, L., et al. 2018, *A&A*, **616**, A132
- Lindgren, L., Bastian, U., Biermann, M., et al. 2021, *A&A*, **649**, A4
- Lomb, N. R. 1976, *Astrophysics and Space Science*, **39**, 447
- Luger, R., Agol, E., Foreman-Mackey, D., et al. 2019, *AJ*, **157**, 64
- Mann, A. W., Newton, E. R., Rizzuto, A. C., et al. 2016, *AJ*, **152**, 61
- Mann, A. W., Johnson, M. C., Vanderburg, A., et al. 2020, *AJ*, **160**, 179
- Masuda, K. 2015, *ApJ*, **805**, 28
- Mazeh, T., Holczer, T., & Shporer, A. 2015, *ApJ*, **800**, 142
- McKinney, W. 2010, in *Proceedings of the 9th Python in Science Conference*, ed. S. van der Walt & J. Millman, 51
- McQuillan, A., Mazeh, T., & Aigrain, S. 2014, *ApJS*, **211**, 24
- Meibom, S., Mathieu, R. D., & Stassun, K. G. 2007, *ApJL*, **665**, L155
- Meibom, S., Barnes, S. A., Latham, D. W., et al. 2011, *The Astrophysical Journal Letters*, **733**, L9
- Meibom, S., Torres, G., Fressin, F., et al. 2013, *Nature*, **499**, 55
- Meingast, S., & Alves, J. 2019, *A&A*, **621**, L3
- Meingast, S., Alves, J., & Rottensteiner, A. 2021, *A&A*, **645**, A84
- Montet, B. T., Tovar, G., & Foreman-Mackey, D. 2017, *ApJ*, **851**, 116
- Morris, B. M. 2020, *ApJ*, **893**, 67
- Morton, T. D., Bryson, S. T., Coughlin, J. L., et al. 2016, *ApJ*, **822**, 86
- Narita, N., Fukui, A., Yamamoto, T., et al. 2020, in *Society of Photo-Optical Instrumentation Engineers (SPIE) Conference Series*, Vol. 11447, Society of Photo-Optical Instrumentation Engineers (SPIE) Conference Series, 114475K

- Newton, E. R., Mann, A. W., Tofflemire, B. M., et al. 2019, *ApJ*, **880**, L17
- Ogihara, M., Morbidelli, A., & Guillot, T. 2015, *A&A*, **578**, A36
- Oh, S., Price-Whelan, A. M., Hogg, D. W., Morton, T. D., & Spergel, D. N. 2017, *AJ*, **153**, 257
- Owen, J. E. 2020, arXiv:2009.03919 [astro-ph], arXiv: 2009.03919
- Owen, J. E., & Wu, Y. 2013, *ApJ*, **775**, 105
- . 2016, *ApJ*, **817**, 107
- Pavlidou, T., Scholz, A., & Teixeira, P. S. 2021, *MNRAS*, **503**, 3232
- Pecaut, M. J., & Mamajek, E. E. 2013, *ApJS*, **208**, 9
- Pecaut, M. J., & Mamajek, E. E. 2016, *MNRAS*, **461**, 794
- Pérez, F., & Granger, B. E. 2007, *Computing in Science and Engineering*, **9**, 21
- Plavchan, P., Barclay, T., Gagné, J., et al. 2020, *Nature*, **582**, 497
- Randich, S., Tognelli, E., Jackson, R., et al. 2018, *A&A*, **612**, A99
- Ratzenböck, S., Meingast, S., Alves, J., Möller, T., & Bomze, I. 2020, *A&A*, **639**, A64
- Rebull, L. M., Stauffer, J. R., Bouvier, J., et al. 2016, *AJ*, **152**, 113
- Reinhold, T., & Hekker, S. 2020, *A&A*, **635**, A43
- Ricker, G. R., Winn, J. N., Vanderspek, R., et al. 2015, *Journal of Astronomical Telescopes, Instruments, and Systems*, **1**, 014003
- Rizzuto, A. C., Mann, A. W., Vanderburg, A., Kraus, A. L., & Covey, K. R. 2017, *AJ*, **154**, 224
- Rizzuto, A. C., Newton, E. R., Mann, A. W., et al. 2020, arXiv:2005.00013 [astro-ph]
- Roccatagliata, V., Franciosini, E., Sacco, G. G., Randich, S., & Sicilia-Aguilar, A. 2020, *A&A*, **638**, A85
- Roettenbacher, R. M., Monnier, J. D., Korhonen, H., et al. 2017, *ApJ*, **849**, 120
- Röser, S., & Schilbach, E. 2020, *A&A*, **638**, A9
- Rowe, J. F., Bryson, S. T., Marcy, G. W., et al. 2014, *ApJ*, **784**, 45
- Rubenzahl, R. A., Dai, F., Howard, A. W., et al. 2021, *AJ*, **161**, 119
- Salvatier, J., Wieckiâ, T. V., & Fonnesbeck, C. 2016, PyMC3: Python probabilistic programming framework
- Sanchis-Ojeda, R., & Winn, J. N. 2011, *ApJ*, **743**, 61
- Scargle, J. D. 1982, *ApJ*, **263**, 835
- Scott, N. J., Howell, S. B., Horch, E. P., & Everett, M. E. 2018, *PASP*, **130**, 054502
- Shapiro, A. I., Solanki, S. K., Krivova, N. A., Yeo, K. L., & Schmutz, W. K. 2016, *A&A*, **589**, A46
- Skrutskie, M. F., Cutri, R. M., Stiening, R., et al. 2006, *AJ*, **131**, 1163
- Soderblom, D. R., Hillenbrand, L. A., Jeffries, R. D., Mamajek, E. E., & Naylor, T. 2014, *Protostars and Planets VI*, 219
- Spake, J. J., Sing, D. K., Evans, T. M., et al. 2018, *Nature*, **557**, 68
- Stassun, K. G., Oelkers, R. J., Paegert, M., et al. 2019, *AJ*, **158**, 138
- Stauffer, J., Rebull, L., Bouvier, J., et al. 2016, *AJ*, **152**, 115
- Stauffer, J. R., Hartmann, L. W., Prosser, C. F., et al. 1997, *ApJ*, **479**, 776
- Stephenson, C. B. 1959, *PASP*, **71**, 145
- Strassmeier, K. G. 2009, *Astronomy and Astrophysics Review*, **17**, 251
- Tenenbaum, P., Christiansen, J. L., Jenkins, J. M., et al. 2012, *ApJS*, **199**, 24
- Theano Development Team. 2016, arXiv e-prints, abs/1605.02688
- Thompson, S. E., Coughlin, J. L., Hoffman, K., et al. 2018, *ApJS*, **235**, 38
- Tian, H.-J. 2020, *ApJ*, **904**, 196
- Tofflemire, B. M., Rizzuto, A. C., Newton, E. R., et al. 2021, *AJ*, **161**, 171
- Ujjwal, K., Kartha, S. S., Mathew, B., Manoj, P., & Narang, M. 2020, *AJ*, **159**, 166
- Van Eylen, V., Albrecht, S., Huang, X., et al. 2019, *AJ*, **157**, 61
- Villa Vélez, J. A., Brown, A. G. A., & Kenworthy, M. A. 2018, *Research Notes of the American Astronomical Society*, **2**, 58
- Vissapragada, S., Knutson, H. A., Jovanovic, N., et al. 2020, *AJ*, **159**, 278, aDS Bibcode: 2020AJ....159..278V
- Vogt, S. S., Allen, S. L., Bigelow, B. C., et al. 1994, SPIE Conference Series, ed. D. L. Crawford & E. R. Craine, Vol. 2198
- Walt, S. v. d., Colbert, S. C., & Varoquaux, G. 2011, Computing in Science & Engineering, **13**, 22
- Wenger, M., Ochsenbein, F., Egret, D., et al. 2000, *A&AS*, **143**, 9
- Yee, S. W., Petigura, E. A., & von Braun, K. 2017, *ApJ*, **836**, 77
- Zari, E., Hashemi, H., Brown, A. G. A., Jardine, K., & de Zeeuw, P. T. 2018, *A&A*, **620**, A172
- Zari, E., Hashemi, H., Brown, A. G. A., Jardine, K., & de Zeeuw, P. T. 2018, *A&A*, **620**, A172
- Zhou, G., Quinn, S. N., Irwin, J., et al. 2021, *AJ*, **161**, 2

## APPENDIX

### A. YOUNG, AGE-DATED, AND AGE-DATEABLE STAR COMPILATION

The v0.6 CDIPS target catalog (Table 3) includes some important updates from previous versions. As in Bouma et al. (2019), we collected membership information for young, age-dated, or age-dateable stars from across the literature. Table 4 gives a list of the sources included, and some brief summary statistics.

The first major important change is that the extent of analyses performed on the Gaia data at the time of our compilation was wide and deep enough that we opted to neglect pre-Gaia analyses, except in cases for which spectroscopically confirmed samples of stars had been collected. The membership lists for instance of Kharchenko et al. (2013) and Dias et al. (2014) (MWSC and DAML) were no longer required, especially given their relatively high field-star contamination rates compared to Gaia-derived membership catalogs.

For any of the catalogs for which Gaia DR2 identifiers were not immediately available, we either followed the spatial (plus proper-motion) crossmatching procedures described in Bouma et al. (2019), or else we pulled the Gaia DR2 source identifiers associated with the catalog from SIMBAD. We consequently opted to drop the `ext_catalog_name` and `dist` columns maintained in Bouma et al. (2019), as these were only populated for a small number of stars.

The most crucial parameters of a given star for our purposes are the Gaia DR2 source identifier (`source_id`), the cluster name (`cluster`), and the (`age`). Given the hierarchical nature of many stellar associations, we do not attempt to resolve the cluster names to a single unique string. The Orion complex for instance, can be divided into almost one hundred kinematic subgroups (Kounkel et al. 2018). Similar complexity applies to the problem of determining homogeneous ages, which we do not attempt to resolve. Instead, we simply merged the cluster names and ages reported by various authors together.

This means that our “age” column can be null, for cases in which the original authors did not report an age, and a reference literature age was not readily available. Nonetheless, since we do generally prefer stars with known ages, we made a few additional efforts to populate this column. When available, the age provenance is from the original analysis of the cluster. However, in a few cases we adopted other ages when the string-based crossmatches on the “cluster” name was straightforward. In particular, we used the ages determined by Cantat-Gaudin et al. (2020) to assign ages to the catalogs from Gaia Collaboration et al. (2018a), Cantat-Gaudin et al. (2018), Castro-Ginard et al. (2020), and Cantat-Gaudin & Anders (2020).

The catalogs we included for which ages were not immediately available were those of Cotten & Song (2016), Oh et al. (2017), Zari et al. (2018), Gagné et al. (2018b), Gagné et al. (2018a), Gagné & Faherty (2018), and Ujjwal et al. (2020). While in principle the moving group members discussed by Gagné et al. (2018b,a); Gagné & Faherty (2018) and Ujjwal et al. (2020) have easily associated ages, our SIMBAD cross-matching lost the moving group association from those studies, which should therefore be recovered tools such as BANYAN  $\Sigma$ .<sup>6</sup> We also included the SIMBAD object identifiers TT\*, Y\*O,Y\*?, TT?, and pMS\*. Finally, we also included every star in the NASA Exoplanet Archive `ps` table that had a Gaia identifier available (Akeson et al. 2013). If the age had finite uncertainties, we also included it, since stellar ages determined through the combination of isochrone-fitting and transit-derived stellar densities typically have higher precision than from isochrones alone.

The technical manipulations for the merging, cleaning, and joining were performed using pandas (McKinney 2010). The eventual crossmatch (using the Gaia DR2 `source_id`) against the Gaia DR2 archive was performed asynchronously on the Gaia archive website<sup>7</sup>.

### B. KINEMATIC SELECTION OF $\delta$ LYR CLUSTER MEMBERS

Figure 6 shows stars reported by Kounkel & Covey (2019) to be in the group “Theia 73”, which was cross-matched by Kounkel & Covey as being “Stephenson 1”. Kounkel & Covey (2019) reported 3,071 stars to be present in this cluster. For our Figure, galactic positions were calculated and plotted only for stars with parallax signal-to-noise exceeding 20. The location of the Sun is shown on the plots. The smattering of reported cluster members (gray and black points) has a significantly different structure than the cluster initially identified by Stephenson (1959) and corroborated by Eggen (1968). While the non-uniform “clumps” might be part of a real structure, they could also be an artifact of the data processing steps performed by Kounkel & Covey (2019). We therefore opted to only consider stars in the immediate kinematic and spatial vicinity of

<sup>6</sup> <http://www.exoplanetes.umontreal.ca/banyan/banyansigma.php>

<sup>7</sup> <https://gea.esac.esa.int/archive/>

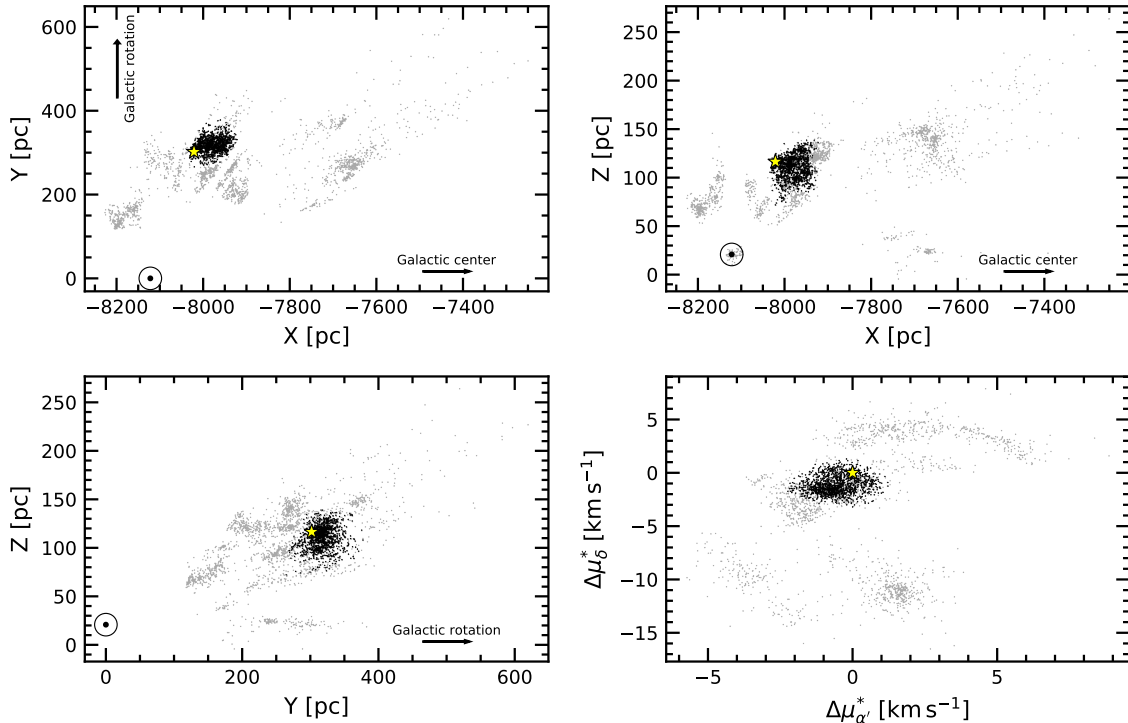


**Figure 6. Galactic position and tangential velocities of the  $\delta$  Lyr cluster.** Points are candidate cluster members with  $\bar{\omega}/\sigma_{\bar{\omega}} > 20$ , reported to be in the group by Kounkel & Covey (2019). We focus on stars in a small region (black points) in the kinematic vicinity of Kepler 1627 (yellow star). The other candidate cluster members (gray points) may or may not share the ages of the selected kinematic group. The location of the Sun is ( $\odot$ ) is shown.

Kepler 1627. The tangential velocities relative to Kepler 1627 are shown in the bottom right panel. These are computed by assuming that every star has the same three-dimensional spatial velocity as Kepler 1627, where we assume a systemic radial velocity of  $-16.7 \pm 0.2 \text{ km s}^{-1}$  based on the reconnaissance spectra obtained by A. Howard on HIRES and D. Latham on TRES. The relevant projection effects are then taken into account, as discussed by *e.g.*, Meingast et al. (2021) and Bouma et al. (2021). We performed the actual selection by then manually drawing lassos with the interactive glue visualization tool (Beaumont et al. 2014) in the four projections shown in Figure 6. While bona fide members likely exist outside of our selection region (and our selection also includes some field star interlopers), our aim is to verify the existence of the cluster in the vicinity of Kepler 1627, and to measure its age. The procedure we have adopted enables both tasks.

### C. BINARITY AND STELLAR ROTATION FOR $\delta$ LYR CLUSTER MEMBERS

Figure 7 shows the rotation-color diagram for  $\delta$  Lyr cluster members, with the points colored according to indicators of binarity. The binaries tend to be redder and have shorter rotation periods. We know of two possible explanations based on selection effects, and two based on physics.

Possible selection effects include *i*) binaries have a component that contributes additional red light to the system, which could skew the color measurement of the primary; and *ii*) the unresolved binary companions could contaminate the rotation period measurement (*e.g.*, Stauffer et al. 2016, Section 5.1).

The two possible physical effects that could be relevant are tidal locking and pre-main-sequence disk locking. Tidal locking has been argued to be an unlikely explanation for the frequency of rapid rotators due to the population statistics; a more likely scenario would be that the presence of the binary leads to faster disk dispersal, enabling the primary to contract to more rapid rotation periods than possible for single stars (Meibom et al. 2007; Bouma et al. 2020).

### D. TRANSIT AND STELLAR VARIABILITY MODEL

#### D.1. Long Cadence Data

We fitted the Kepler nce time series with a model that simultaneously included the planetary transit and the stellar variability. The stellar variability was modelled with the RotationTerm Gaussian Process kernel

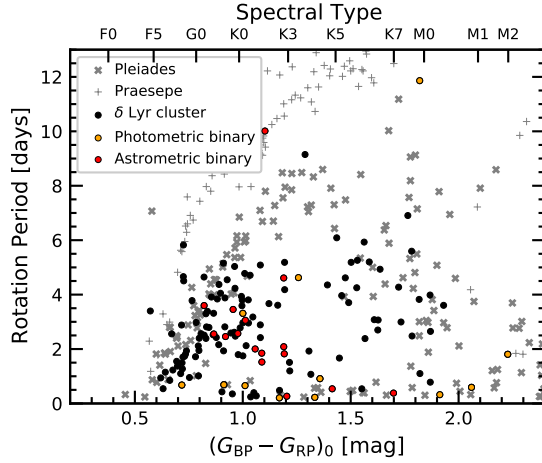


**Figure 7. Binarity indicators for rotators in  $\delta$  Lyr cluster.** Data are as in the lower panel of Figure 2. Astrometric binaries ( $\text{RUWE} > 1.2$ ) appear in red; photometric binaries ( $> 0.3$  mag above an empirical isochrone; 20% of stars) are orange. Over  $0.6 < (G_{\text{BP}} - G_{\text{RP}})_0 < 1.5$ , the detected rotation periods in binaries tend to fall below the slow sequence.

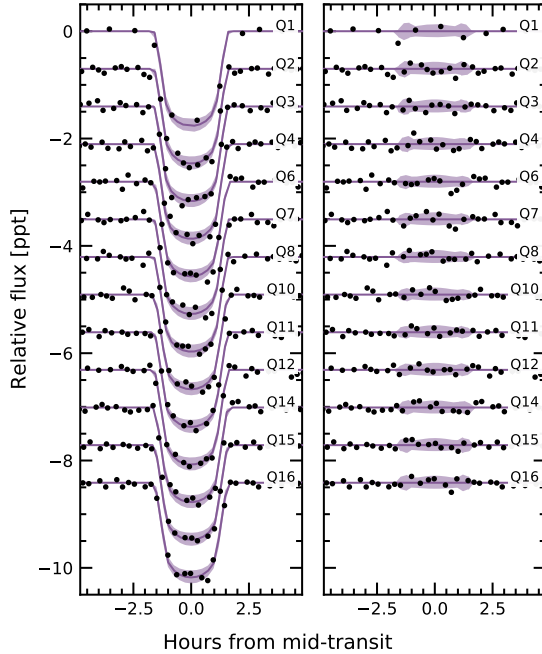


**Figure 8. Transit model residuals through time (binned by Kepler quarter).** *Left:* Phase-folded transit of Kepler 1627b, with stellar variability removed. Black points are binned to 20 minute intervals. The  $2\sigma$  model uncertainties and the maximum *a posteriori* model are shown as the faint purple band, and the dark purple line. *Right:* As on the left, with the transit removed. Quarters 6 and 7 show a consistent deviation in the second half of the transit.

in exoplanet (Foreman-Mackey et al. 2020). This kernel assumes that the variability is generated by a mixture of two damped simple harmonic oscillators with characteristic frequencies set by  $1/P_{\text{rot}}$  and its first harmonic. We additionally incorporated a “jitter” term to inflate the flux uncertainties in a manner that accounted for otherwise unmodelled excess white noise, and let the eccentricity float. For the limb-darkening, we assumed a quadratic law, and sampled using the uninformative prior suggested by Kipping (2013).

Our adopted model therefore included 10 free parameters for the transit ( $\{P, t_0, \log R_p/R_\star, b, u_1, u_2, R_\star, \log g, e \cos \omega, e \sin \omega\}$ ), 2 parameters for the light curve normalization and uncertainty calibration ( $\{\langle f \rangle, \log \sigma_f\}$ ), and 5 hyperparameters for the GP ( $\{\sigma_{\text{rot}}, \log P_{\text{rot}}, \log Q_0, \log dQ, f\}$ ). We also considered including an additive SHOTerm kernel to account for stochastic noise, but found that this did not significantly affect the results, and so opted for the simpler GP kernel. We fitted the models using PyMC3 (Salvatier et al. 2016; Theano Development Team

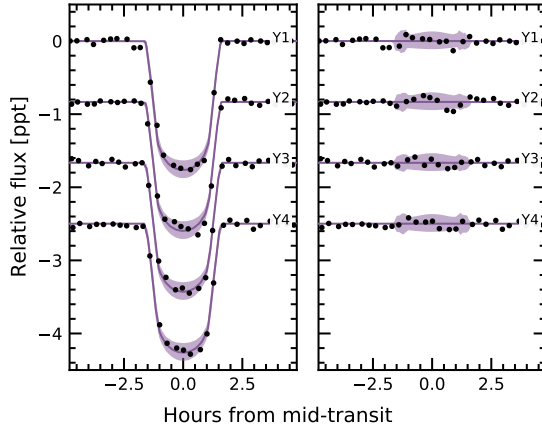


**Figure 9. Transit model residuals through time (binned by year of observation).** *Left:* Phase-folded transit of Kepler 1627b, with stellar variability removed. Points and models are as in Figure 8. *Right:* As on the left, with the transit removed.

2016). After initializing each model with the parameters of the maximum *a posteriori* model, we assumed a Gaussian likelihood, and sampled using PyMC3’s gradient-based No-U-Turn Sampler (Hoffman & Gelman 2014). We used  $\hat{R}$  as our convergence diagnostic (Gelman & Rubin 1992).

Figure 3 shows the resulting model in orange (top) and purple (bottom). While the fit appears reasonably good, an asymmetry is present during the transit: the measured flux is systematically high during the first half, and low in the second half. We verified that this effect is not caused by our stellar variability model by exploring an alternative approach in which we isolated each transit window and locally fitted out polynomial trends, and then binned all the observed transits; the asymmetry was still present, at a comparable amplitude.

Figures 8 and 9 show the Kepler data binned over quarters and years. In Figure 8 Quarter 6 shows the strongest asymmetry out of any of the quarters: a deviation of about 3 ppt from expectation. Quarter 7 shows an anomaly at roughly the same transit phase. Year 2 correspondingly shows the strongest anomaly out of any year in Figure 9.

We considered three possible explanations for the anomaly: gravity darkening, transit timing variations, and spot-crossing events. Gravity darkening is based on the premise that the rapidly rotating star becomes oblate, and brighter near the poles than the equator (e.g., Masuda 2015). The fractional shape change due to gravity darkening is on the order of  $(P_{\text{break}}/P_{\text{rot}})^2$ , for  $P_{\text{break}}$  the break-up rotation period, and  $P_{\text{rot}}$  the rotation period. Using the parameters from Table 2, this yields an expected 1.6% distortion of the  $\approx 1.8$  ppt transit depth: *i.e.*, an absolute deviation of  $\approx 3$  ppm. The observed residual has an amplitude of  $\approx 30$  ppm. Since the expected signal is smaller than the observed anomaly by an order of magnitude, gravity darkening seems to be an unlikely explanation.

The scenario of transit timing variations (TTVs) producing the asymmetry seems unlikely, since the analysis by Holczer et al. (2016) implies that any such variations in Kepler 1627 need to be less than of order minutes. Figures 8 and 9 also provide little evidence in support of this possibility.

The final possibility is that of starspot crossings. Young stars are thought to have higher spot-covering fractions than old stars (e.g., Morris 2020, Plavchan et al. 2020). Young solar-type stars may also host dark starspots at high stellar latitudes (e.g., EK Dra Strassmeier 2009), though interferometric imaging of spotted giant stars has found different starspot latitude distributions than those inferred from Doppler imaging (Roettenbacher et al. 2017). Regardless, for any spot-crossing anomalies to add coherently over the 144 Kepler transits, it seems likely that we would need either for spots to be persistent at a particular latitude (and for a slightly misaligned orbit), or for a “stroboscopic” longitudinal phasing (e.g., Dai et al. 2018). For our system,  $P_{\text{orb}}/P_{\text{rot}} \approx 2.76$ , which means that every 4 transits and 11 stellar rotations, the planet crosses over roughly the same stellar longitude, which could enable the necessary phasing if the spot-groups are long-lived. Unfortunately, the typical S/N per Kepler transit is  $\approx 8$ , which renders individual spot-crossing events unresolved. Therefore, although among the possible ideas starspot crossings seem the most likely to provide the additional photometric scatter observed during transits, our reasoning is essentially that the expected spot-crossing anomaly amplitudes ( $\approx 100$  ppm) could be correct; we are not able to definitely show that this is the correct explanation, and the issue could deserve further exploration.

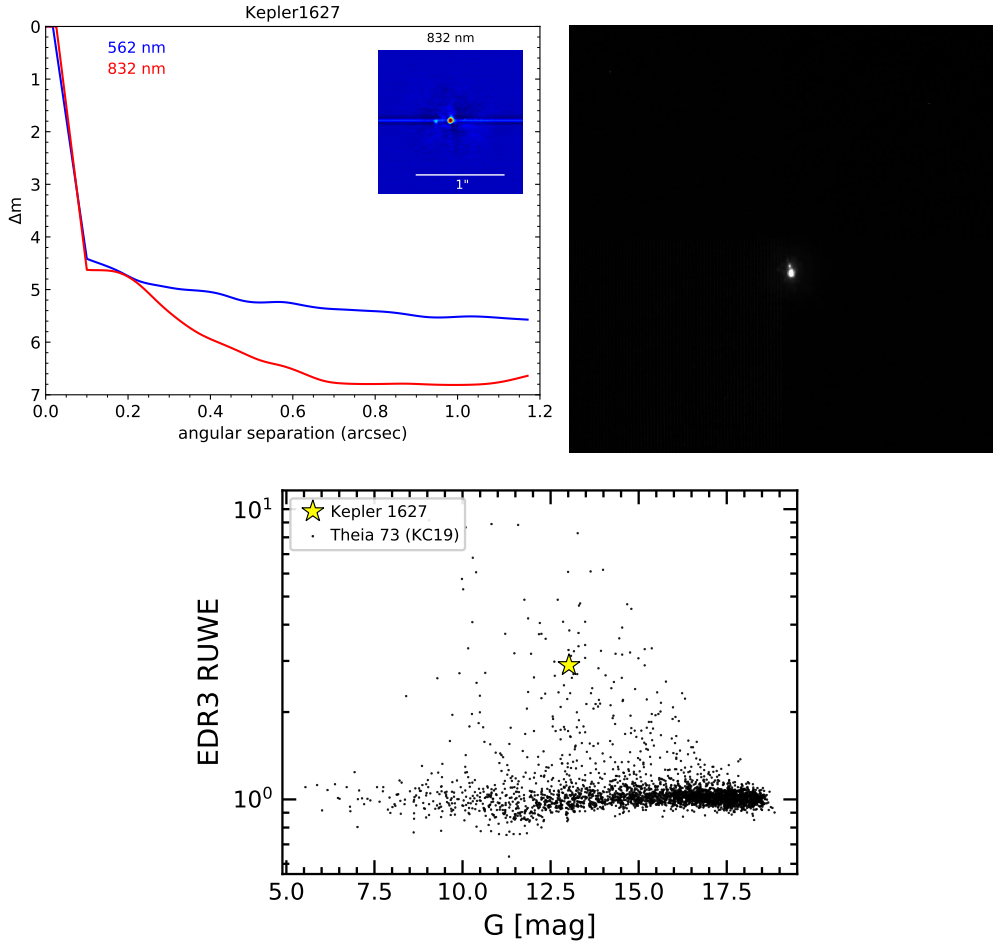


**Figure 10. Kepler 1627 is a binary.** *Top:* High-resolution imaging from Gemini-North/‘Alopeke (*left*) and Keck/NIRC2 (*right*) shows an  $\approx$ M2V companion at  $\rho \approx 0.^{\prime\prime}16$ , which corresponds to a projected separation of  $53 \pm 7$  AU. *Bottom:* Gaia EDR3 renormalized unit weight error (RUWE) point estimates for Kepler 1627A and other members of the  $\delta$  Lyr cluster. Since other members of the cluster with similar colors have comparable degrees of photometric variability, the high RUWE suggests that Kepler 1627 is an astrometric binary.

#### E. COMPANION STAR AND FALSE POSITIVE ASSESSMENT

We first noted the presence of a stellar neighbor in archival Keck/NIRC2 Kp-band adaptive optics imaging ( $2.12 \mu\text{m}$ ), from the Spring semesters of both 2015 and 2019. We acquired additional Gemini-North/‘Alopeke speckle imaging on 24 June 2021, which showed the same companion in the  $0.83 \mu\text{m}$  notch filter, but not the  $0.56 \mu\text{m}$  filter. Figure 10 summarizes the results of the high-resolution imaging. Although the companion is unresolved in the Gaia source catalog, its existence was also suggested by the primary star’s large RUWE, relative to other members of the  $\delta$  Lyr cluster. The images yield a projected separation  $\rho \approx 0.^{\prime\prime}16$ , with  $\Delta m_{832} \approx 3.1$  and  $\Delta m_{Kp} = 2.5$ . Using the measured Gaia EDR3 parallax for the system, this implies a projected separation of  $53 \pm 7$ . Given the low geometric probably of a star imaged within  $\rho \approx 0.^{\prime\prime}16$  to be a chance companion along the line of sight, and the large observed RUWE, we proceed under the assumption that the companion is bound, and that the Kepler 1627 system is binary. Based on the tabulation<sup>8</sup> by Pecaut & Mamajek (2013), the measured magnitude differences for a G8V primary correspond to a spectral type for the companion of  $\approx$ M2V ( $M_* \approx 0.44 M_\odot$ ). However, the companion should have a longer pre-main-sequence contraction phase than the primary, which would imply that this mass is overestimated by  $\sim 10$  to 20%.

Could the companion be creating a false positive signal? The companion star contributes  $\approx 1\%$  of the total flux observed in the Kepler aperture. The observed transit has a depth of 0.18%. An 18% deep eclipse of the

<sup>8</sup> [http://www.pas.rochester.edu/~emamajek/EEM\\_dwarf\\_UBVIJHK\\_colors\\_Teff.txt](http://www.pas.rochester.edu/~emamajek/EEM_dwarf_UBVIJHK_colors_Teff.txt), version 2021/03/02.

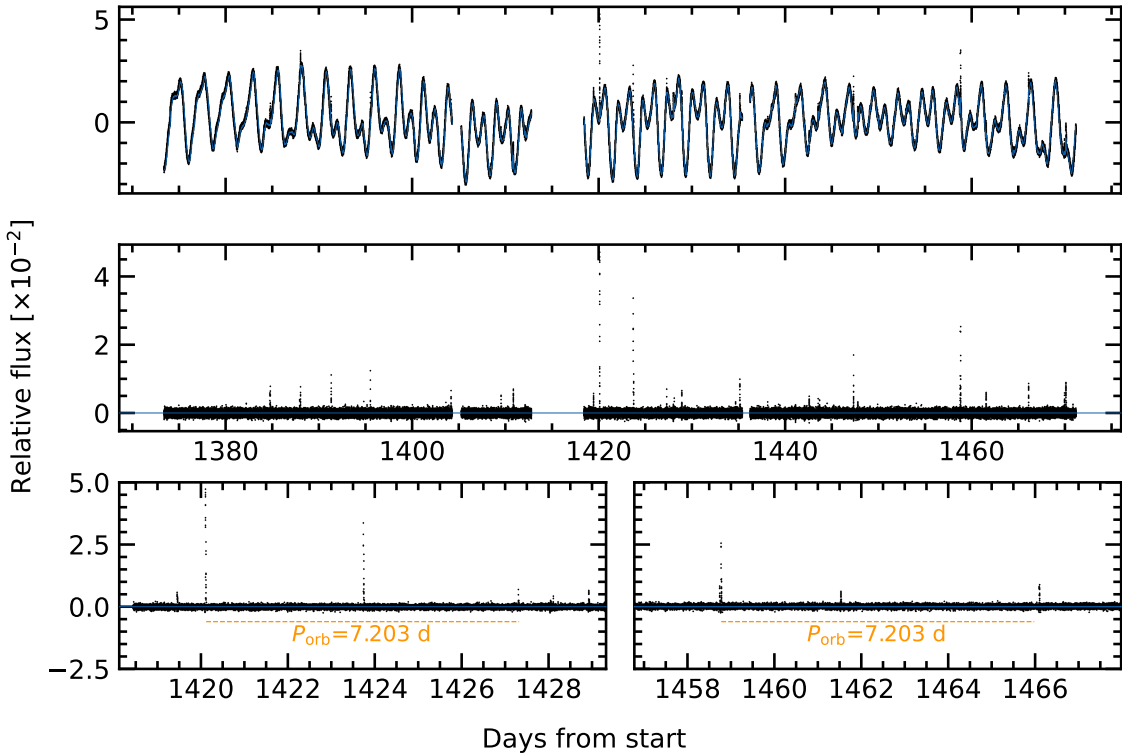


**Figure 11. Flares in Kepler 1627.** *Top:* The full short cadence Kepler dataset, acquired at 1-minute sampling (black points) is shown with a stellar variability model (blue line). *Middle:* Residual after subtracting the stellar variability model. Flares appear as spikes. *Bottom:* Zooms of the brightest, and third-brightest flares. A timing coincidence – that both flares have “successors” approximately one orbital period after the initial event – is emphasized.

secondary star would therefore be needed to produce a signal with the appropriate depth. The shape of the observed signal requires the impact parameter to be below 0.74 (Table 2); the body transiting the secondary would therefore need to be non-grazing with  $R_3/R_2 \approx 0.42$ . Assuming a  $\approx 0.42R_\odot$  radius of the imaged secondary, this would imply a tertiary stellar radius of  $\approx 0.2R_\odot$ . This yields a contradiction: this scenario would require an ingress and egress phase that each span  $\approx 40\%$  of the transit duration ( $\approx 65$  minutes). The actual measured ingress and egress duration is  $\approx 15$  minutes),  $4.4\times$  shorter. The combination of the companion’s brightness, transit depth, and ingress duration therefore rule out the scenario that it could explain the transit signal.

## F. FLARE ANALYSIS

In addition to the 3.9 years of long cadence data, short cadence (1-minute) Kepler observations were acquired over 97.7 days during Quarter 15. The short cadence light curve shows a higher rate of flaring than visible in the long cadence data (Figure 11). We analyzed the short cadence light curve and its flares according to the following procedure.

For cleaning, we performed the following iterative detrending procedure.

1. Model the starspot-induced variability using a Gaussian Process with a SHOTerm kernel (see Section D), a white-noise jitter term, and the mean flux. Fit the model to the time, flux, and flux uncertainty.
2. Select points more than twice the median absolute deviation from the residual, and exclude them from the light curve (these points include the flares). Repeat Step 1.
3. Using the residual from Step 2, identify all flares, requiring them to be at least 20 cadences apart, at least 7 median absolute deviations above the median baseline, and lasting at least 2 cadences in duration. Build the mask spanning these times, from 5 minutes before each flare begins to 2.5 minutes after the final flare cadence. Repeat Step 1 a final time.

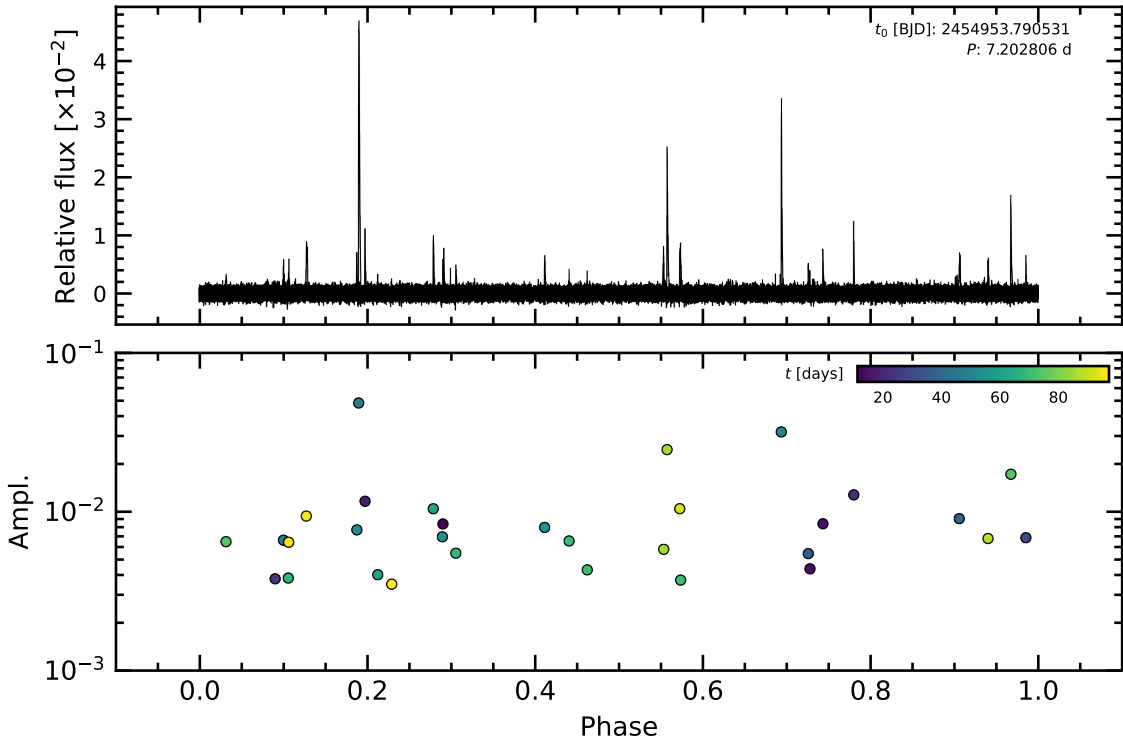


**Figure 12. Phase-folded flares in Kepler 1627.** *Top:* As in the middle of Figure 11, phase-folded at the planet’s ephemeris. *Bottom:* Fitted flare amplitudes and orbital phases – each point represents one flare. Colors indicate relative time, from the beginning of the 98-day short cadence Quarter 15 dataset (dark blue) to the end (light yellow). Lower amplitude flares likely exist in the data, and were not examined.

The flares were identified and fitted using `altaipony` (Davenport 2016; Ilin et al. 2021). The analytic flare model is from Davenport et al. (2014) and it parametrizes the flare with a start time, an exponential lag time, and an amplitude. Figure 12 shows the resulting flares, amplitudes, and phases.

There were  $N_f = 24$  flares that exceeded 0.5% in relative flux during the short cadence observations. These 24 flares spanned a total of 6.5 hours ( $\sim 15$  minutes per flare). Whether it is meaningful or not, we noticed a coincidence in the flare arrival times. The coincidence is that despite the low flare duty cycle, one orbital period after the brightest flare, a second flare followed. This and a similar event are shown in Figure 11. The timing error is good to a  $\approx 0.2\%$  difference from the orbital period, which given the duty cycle seems *a priori* unlikely. If we consider flares falling within 2% of the planet’s orbital period after a previous flare, then 4 of the 24 flare events have candidate “successors”.

As with any coincidence, if one does not have a firm prediction, it is difficult to assess the statistical significance of a surprise. Since our surprise was specifically at the inter-arrival time of certain flares coinciding with special time intervals, we performed the following analysis. First, we considered all unordered pairs of flares. For  $N$  flares there are  $\binom{N}{2}$  such pairs (for our case, 276 pairs). We then compared the distribution of the pair separations against that from a Poisson distribution. Specifically, we drew  $N_f = 24$  samples from a Poisson distribution with  $\lambda = \Delta t / N_f$ , for  $\Delta t = 97.7$  days the duration of the observations, and repeated the draw  $10^3$  times with unique random seeds.

Figure 13 shows the results. The vertical lines in the figure show the planetary orbital period, the synodic period  $P_{\text{syn}} = (P_{\text{rot}}^{-1} - P_{\text{orb}}^{-1})^{-1}$ , and linear combinations thereof. Note that the tidal period (half the synodic period) is not shown. The bins are logarithmically spaced to give 100 bins between the minimum and maximum ordinate values. The gray bands express the range of values observed from the Poissonian draws. While it does seem like a rather odd coincidence for peaks in the observed flare arrival time distribution to coincide with the locations of these “special intervals”, the statistical evidence for a non-Poissonian process driving the flares does not seem especially strong. More quantitatively, the peaks observed at the orbital and synodic periods are within the  $\pm 2\sigma$  range of a Poissonian process, and those at  $P_{\text{orb}} + P_{\text{syn}}$  and  $P_{\text{orb}} + 2P_{\text{syn}}$  are only slightly above this range. With that said, future analyses of these data by investigators more versed in this topic than ourselves could very well yield more detailed insights.

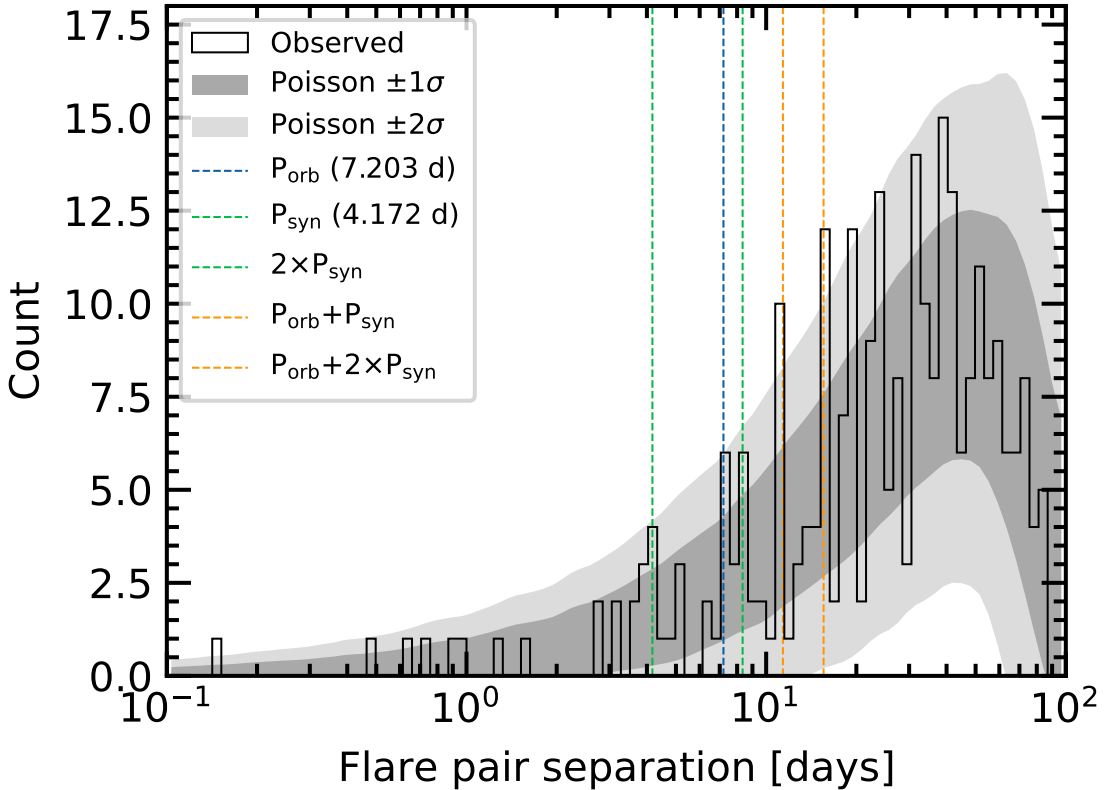


**Figure 13. Statistics of inter-flare arrival times.** 24 flares were recorded with amplitudes exceeding 0.5% over the 97.7 days of short cadence observations. The histogram of the time intervals between every possible pair of flares is shown in black. Some plausibly important timescales for star-planet interactions, namely the planetary orbital period and synodic period (the orbital period as seen from the rotating stellar frame) are shown along with their linear combinations. Monte Carlo draws from a Poisson distribution are shown with the gray bands. While peaks in the observed distribution do coincide with the locations of these “special periods”, the statistical evidence for a non-Poissonian process driving the flares does not reach the  $5-\sigma$  threshold.